HHS Public Access

Author manuscript

Neuron. Author manuscript; available in PMC 2022 September 15.

Published in final edited form as:

Neuron. 2021 September 15; 109(18): 2914–2927.e5. doi:10.1016/j.neuron.2021.08.030.

Signature morpho-electric, transcriptomic, and dendritic properties of human layer 5 neocortical pyramidal neurons

Brian E. Kalmbach[1,2,10,*], **Rebecca D. Hodge**[1], **Nikolas L. Jorstad**[1], **Scott Owen**[1], **Rebecca de Frates**[1,#], **Anna Marie Yanny**[1], **Rachel Dalley**[1], **Matt Mallory**[1], **Lucas T. Graybuck**[1,^], **Cristina Radaelli**[1], **C. Dirk Keene**[3], **Ryder P. Gwinn**[4], **Daniel L Silbergeld**[5], **Charles Cobbs**[6], **Jeffrey G Ojemann**[7,8], **Andrew L Ko**[7,8], **Anoop P Patel**[7], **Richard G. Ellenbogen**[7], **Trygve E. Bakken**[1], **Tanya L. Daigle**[1], **Nick Dee**[1], **Brian R. Lee**[1], **Medea McGraw**[1], **Philip R. Nicovich**[1], **Kimberly Smith**[1], **Staci A. Sorensen**[1], **Bosiljka Tasic**[1], **Hongkui Zeng**[1], **Christof Koch**[1], **Ed S. Lein**[1,7], **Jonathan T. Ting**[1,2,9,*]

[1]Allen Institute for Brain Science, Seattle, WA 98109, USA

[2]Department of Physiology and Biophysics, University of Washington, Seattle, WA 98195, USA

[3]Dept. of Pathology, Univ. of Wash., Seattle, WA 98195 USA.

[4]Epilepsy Surgery and Functional Neurosurgery, Swedish Neuroscience Institute, Seattle, WA 98122, USA

[5]Dept. of Neurological Surgery and Alvord Brain Tumor Center, University of Washington, Seattle WA 98195, USA.

[6]The Ben and Catherine Ivy Center for Advanced Brain Tumor Treatment, Swedish Neuroscience Institute, Seattle, WA 98122, USA

[7]Department of Neurological Surgery, University of Washington School of Medicine, Seattle, WA 98195, USA

[8]Regional Epilepsy Ctr., Harborview Med. Ctr., Seattle, WA 98104, USA.

[9]The Washington National Primate Research Center, University of Washington, Seattle, WA 98195, USA

[10]Lead contact

[*]Correspondence: briank@alleninstitute.org and Jonathant@alleninstitute.org.
[^]Current address: Allen Institute for Immunology, Seattle, WA 98109, USA
[#]Current address: Center for Neuroscience, University of California at Davis, Davis, CA 95618, USA

Author contributions: Conceptualization and management of the project: B.E.K., E.S.L. and J.T.T.; Patch-seq and dendritic recording and analysis: B.E.K.; mFISH data generation and analysis: R.D.H., A.M.Y.; RNA-seq data generation and analysis: K.S., R.D.H, N.L.J., T.E.B., S.O., B.T.; histology: M.M., R.DF.; imaging: P.R.N., R.DF.; neuron 3D reconstruction and analysis: R.DF., S.A.S., R.D., M.M.; data visualization tools: L.T.G, B.T.; AAV vectors: T.L.D., J.T.T., L.G., B.T.; neurosurgery and human surgical tissue acquisition: R.P.G., D.L.S., C.C., J.G.O., A.L.K., C.D.K., A.P.P, R.G.E.; manuscript preparation: B.E.K., S.O, and J.T.T. with input from all authors. Program leadership: E.S.L., H.Z., and C.K.

Declaration of Interests: L.T.G., T.L.D., J.T.T., E.L., B.K., H.Z. and B.T. are inventors on a PCT application (PCT/US2019/059927) related to this work. All authors declare no other competing interests.

Summary

In the neocortex, subcerebral axonal projections originate largely from layer 5 (L5) extratelencephalic-projecting (ET) neurons. The unique morpho-electric properties of these neurons have mainly been described in rodents, where retrograde tracers or transgenic lines can label them. Similar labeling strategies are infeasible in the human neocortex, rendering the translational relevance of findings in rodents unclear. We leveraged the recent discovery of a transcriptomically-defined L5 ET neuron type to study the properties of human L5 ET neurons in neocortical brain slices derived from neurosurgeries. Patch-seq recordings, where transcriptome, physiology and morphology were assayed from the same cell, revealed many conserved morpho-electric properties of human and rodent L5 ET neurons. Divergent properties were often subtler than differences between L5 cell types within these two species. These data suggest a conserved function of L5 ET neurons in the neocortical hierarchy, but also highlight phenotypic divergence possibly related to functional specialization of human neocortex.

In brief

Transcriptomics identifies a human L5 neuron corresponding to extratelencephalic projecting neurons in mouse neocortex. Patch-seq recordings from this cell type reveal many conserved and divergent morpho-electric features of L5 ET neurons in human cortex.

Graphical Abstract

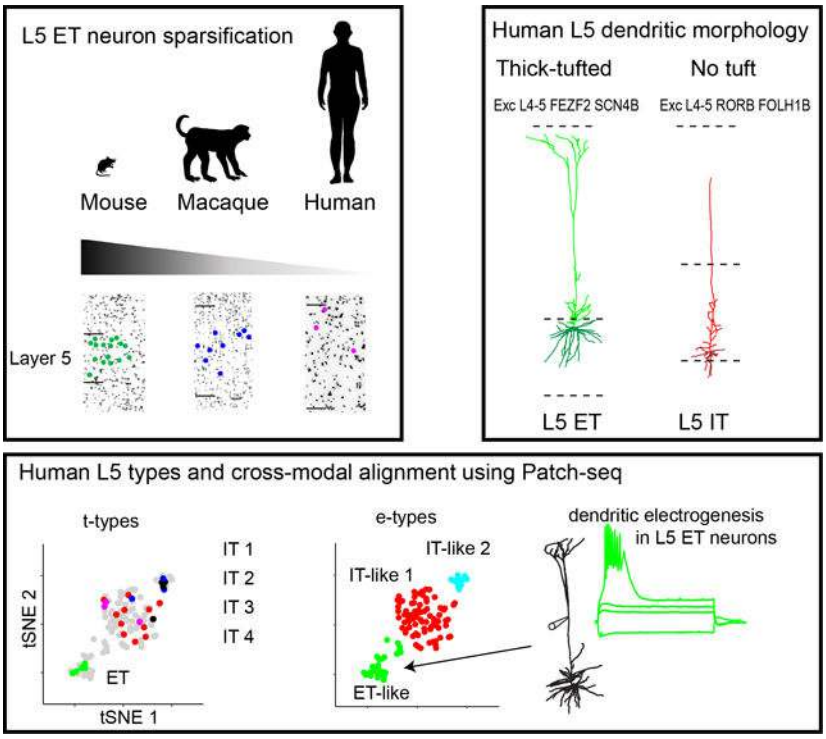

Introduction

Understanding cellular diversity and the specific contributions of distinct cell types to brain connectivity and function is one of the biggest challenges in neuroscience (Zeng and Sanes, 2017). Neocortical pyramidal neurons display an astonishing diversity in gene expression, morphology and physiology (Gouwens et al., 2019; Markram et al., 2015; Sugino et al., 2006; Tasic et al., 2018). One seminal discovery shed light on the organizational structure of excitatory neuron populations by demonstrating that they can be segregated based on their long-range axonal targets (Harris and Shepherd, 2015). This is exemplified in layer 5 (L5) where pyramidal neurons can be broadly segregated into two classes based on whether their long-range axons project only within the telencephalon or both within and outside of the telencephalon (Baker et al., 2018).

Both intratelencephalic-projecting (IT) and extratelencephalic-projecting (ET) neurons send axonal projections within the telencephalon (i.e. the cerebral cortex, basal ganglia, etc.), but only ET neurons project to subcerebral targets (e.g. spinal cord, pons, thalamus). Thus, cortical activity that directly affects subcerebral processing/behavior is routed largely through L5 ET neurons. In rodents, L5 ET neurons have distinctive morpho-electric properties, gene expression, local synaptic connectivity, long-range afferents and response to neuromodulators (Anastasiades et al., 2018; Avesar and Gulledge, 2012; Brown and Hestrin, 2009; Dembrow et al., 2010, 2015; Gouwens et al., 2019; Groh et al., 2010; Guan et al., 2015; Hattox and Nelson, 2007; Kalmbach et al., 2013; Kawaguchi, 2017; Kim et al., 2015; Mao et al., 2011; Sheets et al., 2011; Sorensen et al., 2015; Tasic et al., 2018). Classically, L5 ET neurons possess thick apical dendritic tufts in L1 whereas L5 IT neurons are thin tufted or tuftless. Additionally, compared with L5 IT neurons, L5 ET neurons have properties consistent with enriched HCN channel expression and exhibit strong dendritic electrogenesis (Larkman and Mason, 1990; Mason and Larkman, 1990; Ramaswamy and Markram, 2015; Stuart and Sakmann, 1994; Schiller et al., 1997; Williams and Stuart, 2000). Emerging evidence indicates that these morpho-electric differences result in unique firing properties *in vivo* and that L5 ET and IT neurons contribute to different aspects of perception and behavior (Economo et al., 2018; Kim et al., 2015; Li et al., 2015; Rojas-Piloni et al., 2017; Saiki et al., 2017, Takahashi et al., 2020).

Translating these findings from work in rodents to the human neocortex is complicated by several factors. First, there are major species differences in the gross-laminar organization of the neocortex, the size of neurons, the laminar expression of genes, and the intrinsic membrane properties of homologous cell types (Beaulieu-Laroche et al., 2018; Berg et al., 2020; Hodge et al., 2019; Kalmbach et al., 2018; Mohan et al., 2015; Zeng et al., 2012). Additionally, in rodents, retrograde tracers or viruses can be applied *in vivo* to label L5 ET neurons to target them for patch-clamp physiology or other functional studies (Dembrow et al., 2010; Hattox and Nelson, 2007; Tervo et al., 2016), but these approaches are not possible in humans. Recent advances from single cell transcriptomics offer a unique anchor to identify L5 ET neurons in the human neocortex and to study their cellular properties. We leveraged these recent advances to address which distinguishing cellular properties of rodent L5 ET neurons are conserved or divergent in the human neocortex.

Results

Species differences in the relative abundance of putative L5 ET neurons

In mice, single-cell transcriptomes readily distinguish L5 ET versus IT neurons. Combined retrograde labeling and single cell RNA-sequencing (scRNA-seq; i.e. Retro-seq) has validated this target/transcriptome relationship (Economo et al., 2018; Tasic et al., 2016, 2018). Alignment of human and mouse neocortical taxonomies based on sc/single nucleus(sn) RNA-seq has enabled strong inference of homologous transcriptomic cell types in the human cortex that correspond to L5 ET neuron types in the mouse (Bakken et al., 2020; Hodge et al., 2019, 2020). This alignment revealed a striking species difference in the relative abundance of transcriptomically-defined ET neurons. While the abundance of L5 ET neurons can vary across neocortical region, they are relatively rarer in human compared with rodent neocortex regardless of region (Bakken et al., 2020; Hodge et al., 2019, 2020). sc/snRNA-seq and multiplex fluorescence *in situ* hybridization (FISH) experiments indicate that ET neurons comprise only 2–6% of excitatory neurons in L5 of the human neocortex compared to 20–30% in mice. It is unclear, however, whether the relative rarity of L5 ET neurons is a unique property of the human neocortex. To address this question, we quantified the relative abundance of L5 ET neurons in mouse, macaque and human temporal cortex using RNA FISH probes against conserved L5 ET marker genes (*FAM84B and POU3F1* in separate experiments) and a glutamatergic neuron marker (*SLC17a7*; Figure 1A; Figure S1). In each species, neurons that expressed both *FAM84B/POU3F1 and SLC17a7* were characterized by large pyramidal shaped somata (Figure 1B; Figure S1C). There were also large pyramidal neurons in layer 3 of human and macaque neocortex, but these neurons were negative for *FAM84B* and *POU3F1* (Figure S1D), suggesting that ET neurons are restricted to infragranular layers. For human temporal cortex there was considerable donor-to-donor variability in the thickness of the cortical layers and in the distribution of ET neurons within L5 (Figure S2). Regardless, putative L5 ET neurons were most abundant in mice, followed by macaque and then human temporal cortex (Figure 1C) and the estimates of abundance were highly similar for each species regardless of the marker gene used (*FAM84B* or *POU3F1*).

The identification of a conserved class of transcriptomically defined L5 ET neurons permitted us to identify genes that may contribute to conserved properties of this cell type as well as genes potentially contributing to phenotypic divergence. To identify genes enriched in human L5 ET neurons compared with human L5 IT neurons, we analyzed an existing snRNA sequencing dataset from human middle temporal gyrus (MTG; Hodge et al., 2019). For cross-species comparisons we utilized a published scRNA-seq dataset derived from two brain regions, the mouse primary visual cortex (VISp) and the anterior lateral motor cortex (ALM; Tasic et al. 2018). We identified 4,143 genes with at least 0.5 $\log_2$ fold enriched expression in transcriptomically-defined L5 ET neurons relative to L5 IT neurons in human MTG. Additionally, 477 DE genes were enriched in mouse L5 ET neurons in both VISp and ALM. This gene set was highly enriched for genes associated with axon guidance and synaptic function (Figure 1D and E; red). A notable example includes *BCL11B*, which is required for subcerebral axonal targeting (Arlotta et al., 2005). There were also noteworthy examples of human specific L5 ET genes (Figure 1D and E; blue), including *GRIK1*,

which encodes the ionotropic glutamate receptor, GluR5. Nonetheless, these data suggest that known phenotypes of rodent L5 ET neurons, such as subcerebral axonal targeting are broadly conserved in the human L5 ET transcriptomic cell type.

In rodents, L5 ET neurons express a specific repertoire of ion channels, which contributes to their specialized physiological properties (Baker et al., 2018). Many of these channels are also targets of neuromodulation. Indeed, the response to various neuromodulators differs between L5 ET and IT neurons in rodents (Dembrow and Johnston, 2014). We therefore identified ion channel and neuromodulator receptor-related genes enriched in transcriptomically-defined L5 ET neurons in the human MTG (Figure 1F–G). Many, but not all, of these genes were enriched in mouse L5 ET neurons in both VISp and ALM. In addition to a major pore forming HCN-channel subunit (*HCN1*), several classes of G-protein-coupled receptors (GPCRs) were also enriched in transcriptomically defined L5 ET neurons in human MTG. Many of these GPCRs are associated with neuromodulators that differentially affect L5 ET versus L5 IT neurons in the rodent. For example, we observed species differences in the expression of genes encoding 5-HT1 receptor family subunits (Figure 1G). In mouse L5 ET neurons, *HTR1A* and *HTR1F* were the dominantly expressed subunits, whereas in human L5 ET neurons, *HTR1E* (which is absent in the mouse genome) and *HTR1F* were highly expressed, with little *HTR1A* expression. These data suggest that human and rodent L5 ET neurons likely share some similar distinctive intrinsic membrane properties and responses to neuromodulation in comparison to neighboring L5 IT neuron types. In contrast, cross-species gene expression differences among L5 ET neurons in mouse versus human highlight areas of potential phenotypic divergence.

Distinctive membrane properties of transcriptomically defined L5 ET neurons

The transcriptomic classification of cell types is remarkably predictive of physiological, morphological, and anatomical properties in both human and mouse neocortex (Bakken et al. 2020; Berg et al., 2020; Economo et al., 2018; Gouwens et al., 2020; Scala et al., 2020; Tasic et al., 2018). We therefore predicted that in human MTG the electrophysiological properties of transcriptomically defined L5 ET neurons would differ from neighboring IT neurons in a manner consistent with previous observations in rodents. To test this hypothesis, we performed patch clamp recordings from L5 pyramidal neurons in acute brain slices prepared from neurosurgical resections of human MTG. For a subset of experiments, we performed Patch-seq analysis in which the nucleus was extracted after concluding whole cell recording and then processed for snRNA-seq. The expression levels of thousands of genes were used to assign a transcriptomic cell type identity to the physiologically probed cell by mapping to a reference human MTG transcriptomic cell type taxonomy (Figure 2A). We grouped Patch-seq sampled neurons and non-Patch-seq sampled neurons into electrophysiologically defined types (e-types) based on their aggregate neurophysiological signatures. We then asked whether physiologically defined neurons corresponded to genetically defined L5 ET and IT neuron types determined by Patch-seq mapping.

Using this approach, we obtained 20 Patch-seq samples that mapped with high confidence to one of several infragranular IT types and 5 samples (in green) that mapped to the sole

L5 ET cluster in the reference human MTG transcriptomic cell type taxonomy (Figure 2B). Patch-seq samples mapping to L5 ET and IT types were enriched for multiple established marker genes for the respective types (Figure 2C). Transcriptomically defined L5 ET and IT neurons displayed multiple pairwise differences in intrinsic properties (Figure S3), which we enumerate below. Using unsupervised hierarchical clustering based on physiology, we observed three distinct types of human L5 neurons (Figure 2D). To visualize the collective differences in the properties of these physiologically defined neuron types we used t-distributed stochastic neighbor embedding (t-SNE) for dimension reduction, where the distance between cells approximates differences in physiological properties and thus cells with similar physiological properties cluster together (Figure 2E). All transcriptomically defined L5 ET neurons belonged to one physiologically defined neuron type whereas all transcriptomically defined L5 IT neurons belonged to one of two different physiologically defined cell types (Figure 2F). For simplicity, we refer to these physiologically defined cell types as ET-like, IT-like 1 and IT-like 2, based on their correspondence to transcriptomic cell types and their broad similarity to rodent L5 ET and IT neurons (see below). Notably, the two L5 IT-like physiologically defined cell types were largely enriched for different L5 IT transcriptomic cell types. Thus, there was a strong correspondence between physiologically and transcriptomically defined cell types.

Electrophysiological differences in human L5 ET and IT neurons

The transcriptomically defined L5 ET and IT neurons in human MTG possess distinct electrophysiological properties. To address which physiological features contributed to the clustering of genetically defined L5 ET and IT neuron types, we made pairwise comparisons of specific features between the physiologically and transcriptomically defined cell types.

In rodents, subthreshold properties, especially those related to HCN channel expression, readily distinguish L5 ET from IT neurons across several brain regions (Dembrow et al., 2010; Kalmbach et al., 2013; Sheets et al., 2011; Ramaswamy 2015; Larkman 1990). Notably, *HCN1*, which encodes a major HCN channel pore forming subunit (Robinson and Siegelbaum, 2003), was enriched in transcriptomically defined L5 ET neurons relative to IT neurons in both mouse and human (Figure 1F). Thus, we predicted that HCN-channel related properties would distinguish L5 ET from L5 IT neurons in human MTG. To extract HCN-dependent properties, we measured the voltage response to a series of hyperpolarizing and depolarizing current steps as well as a chirp stimulus (Figure 2A; Figure 3A,B,E; Figure S4).

We observed several differences in HCN channel-related subthreshold membrane properties between transcriptomically/physiologically defined L5 ET and IT neurons. L5 ET-like neurons had a higher resonant frequency, resonant strength, and 3 dB cutoff than both L5 IT-like neuron types (Figure 3C and D; Figure S4). Similarly, the voltage response of L5 ET neurons, but not IT neurons, led the chirp current injection for low frequency components (Figure S4). L5 ET-like neurons also had a lower input resistance and more pronounced voltage sag/rebound than IT-like neurons (Figure 3F–G; Figure S4). Notably, compared with IT-like 1 neurons, IT-like 2 neurons had ~2 fold higher input resistance and a larger rebound potential. Furthermore, as reported in rodents, plotting resonance frequency as a

function of input resistance segregated the neuron types well (Figure 3H; Dembrow et al., 2010; Kalmbach et al., 2015). Importantly, these HCN-related properties were also different between transcriptomically defined L5 ET and IT neurons (Figure 3; Figure S3), thus demonstrating strong correspondence between physiological and transcriptomic definitions of cell types.

In addition to subthreshold differences, rodent L5 ET and IT neurons display several differences in suprathreshold membrane properties (Dembrow et al., 2010; Guan et al., 2015; Hattox and Nelson, 2007; Kalmbach et al., 2013; Oswald et al., 2013; Otsuka and Kawaguchi, 2008; Suter et al., 2013). Action potential properties were extracted from the voltage response to a series of 1 s step current injections of increasing amplitude (Figure 2A). L5 ET-like neurons, perhaps due in part to their low input resistance, displayed the shallowest input/output curves, followed by IT-like and IT-like 2 neuron types (Figures 4A and B). Additionally, L5 ET-like neurons tended to respond to near threshold current injections with a high frequency burst of action potentials (Figure 4A), a phenomenon that has been associated with dendritic Ca^{2+} electrogenesis (Beaulieu-Laroche et al., 2018; Larkum et al., 1999; Shai et al., 2015). To illustrate this behavior, we plotted the first instantaneous firing rate (1/first interspike interval) as a function of the amplitude of the current injection above rheobase (Figure 4C). Putative L5 ET neurons displayed the highest instantaneous firing frequencies for at threshold current injections. Additionally, we calculated the percentage of action potentials that occurred within 50 ms of the first spike during the first current step that produced at least 5 spikes. L5 ET-like neurons had the largest percentage of spikes within 50 ms of the first spike and the highest maximum instantaneous firing rate during this current injection (Figure 4D).

There were many other differences in action potential properties between putative L5 ET and IT neurons in human MTG that mirror differences observed in rodent neocortex. Example single action potentials and phase-plane plots are presented in Figure 4E. Like rodent L5 ET neurons (Dembrow et al., 2010; Pathak et al., 2016; Suter et al., 2013) human L5 ET-like neurons had fast, narrow action potentials characterized by a fast depolarization/repolarization rate, low voltage threshold and narrow width at half-maximum amplitude (Figure 4F–I; Figure S4). Notably, IT-like 2 neurons had similarly fast and narrow action potentials compared to IT-like 1 neurons (Figure 4F–I; Figure S4). ET-like neurons also had the largest amplitude medium afterhyperpolarization potentials (AHP), and the highest variability in spike timing (Figure S4), perhaps due in part to enriched expression of channels contributing to AHPs and their propensity to burst (Guan et al., 2015). As with subthreshold properties, many suprathreshold properties were also different between transcriptomically defined L5 ET and IT neurons (Figure 4; Figure S3), again demonstrating strong correspondence between transcriptomic and physiological definitions of cell types.

As a second approach to investigating which physiological features distinguished between L5 ET-like and IT-like neurons, we trained a series of random forest classifiers on varying subsets of the dataset (Figure S5A). Classifiers had an average accuracy of ~95% when using 40% of the recorded neurons in training and maintained close to this level when using as little as 10% of the dataset. Subthreshold features related to passive membrane properties and HCN conductance had the greatest importance (Figure S5B). The performance of

random forest classifiers only marginally decreased when just the top 10 most important features were used in training (Figure S5C). Furthermore, the general shape of t-SNE projections was robust to the removal of several physiological features (Figure S5D,E). This is consistent with the observation that there are many statistically significant differences between the groups, especially between L5 ET neurons and IT-like 1/2 neurons (Figures 2–4; Table S2). Notably, removing features related to the FI curve collapsed IT-like 1 and IT-like 2 neurons in the tSNE. The FI curve of IT2-like neurons was very different from ET-like and IT-like 1 neurons (see effect sizes, Table S2), which might explain the large linkage distances in the cluster dendrogram (Figure 2D). Nonetheless, these data suggest that subthreshold membrane properties best discriminate between L5 ET and IT neurons, but that several other features are sufficient to classify these cell types.

Putative L5 ET neurons in human MTG have thick-tufted apical dendrites

Rodent L5 ET neurons can be distinguished from L5 IT neurons by their thick apical tuft dendrites (Baker et al., 2018; Gao and Zheng, 2004; Gouwens et al., 2019; Hattox and Nelson, 2007; Larkman and Mason, 1990; Oswald et al., 2013). To determine whether human L5 ET-like neurons possess an apical tuft, we performed dendritic reconstructions of physiologically defined neurons. For comparative purposes we also performed dendritic reconstructions of L5 IT-like neurons (Table S3). Compared with L5 IT-like neurons, L5 ET-like neurons possess a definite apical tuft terminating at the pial surface, but with the tuft branches starting at different distances from the soma (Figure 5A,B). The total length of the apical and basal dendrites was greater in L5 ET neurons compared with IT-like neurons (Figure 5C). Furthermore, L5 ET-like neurons possessed more apical and basal dendritic branches (Figure 5D). Finally, the average diameter of the apical dendrite was larger in L5 ET neurons than L5 IT neurons. As a result of these differences, the total apical and basal dendrite surface area was greater in L5 ET neurons compared with L5 IT neurons (Figure 5F).

In many rodent cortical areas, L5 ET neuron somata are larger and have a larger initial apical shaft compared with L5 IT neurons (Gao and Zheng, 2004; Larkman and Mason, 1990; Oswald et al., 2013). To quantify the somatic shape of human L5 neurons, we measured the height and width of the somata as well as the width of the initial apical dendrite shaft of biocytin filled neurons (Figure 5G–J). In contrast to L5 IT-like neurons, L5 ET-like neuron somata were taller than they were wide. Similarly, the initial apical shaft was wider in ET-like neurons compared with IT-like neurons. These properties gave L5 ET-like neuron somata a distinctive elongated shape that was readily discernable during patch-clamp experiments.

Dendritic electrogenesis in human L5 ET-like neurons

To directly test whether the dendrites of human L5 ET neurons display electrogenesis as suggested by their propensity to fire in bursts, we made whole cell recordings from the dendrites of L5 neurons in human MTG. Example voltage responses to hyperpolarizing and depolarizing current injections measured at different distances from the soma of different neurons are shown in Figure 6A. For a subset of these dendritic recordings, we performed subsequent whole cell recordings from the soma through a second pipette. Projecting the

physiological features recorded at the soma onto a tSNE plot revealed that the dendritically probed neurons were L5 ET-like neurons by this classification (compare Figure 6B to Figure 2E).

We first asked whether the subthreshold membrane properties of human L5 ET-like neurons vary with distance from the soma, as observed in many rodent L5 ET neurons (Dembrow et al., 2015; Kalmbach et al., 2013, 2015, 2017). In contrast to rodent neurons, where input resistance decreases with distance from the soma, input resistance in human L5 neurons increased slightly as a function of distance from the soma (Figure 6C). Additionally, sag ratio and rebound potential were more prominent at distal recording sites (Figure S6) while resonance frequency, 3dB-cutoff and total inductive phase increased as a function of recording distance (Figure S6). Thus, as in many rodent L5 ET neurons, many HCN-related properties were more prominent at distal dendritic recording sites.

In response to depolarizing current injections, we observed prolonged, all-or-nothing plateau potentials in L5 ET-like dendrites (examples from separate neurons are shown in Figure 6A). The width and area under the curve of the spikes increased with distance from the soma, whereas the maximum rate of rise decreased (Figure 6D–F). Intriguingly, the current required to evoke a plateau potential did not vary with distance from the soma and was similar to the current required to elicit a somatic action potential via somatic current injection (Figure 6G). These observations suggest that human L5 ET neurons possess active mechanisms capable of generating dendritic spikes.

Cross-cell type variability is greater than cross-species variability

These data suggest that the defining physiological properties of human L5 ET neurons are broadly like those reported in rodent neocortex. To directly compare somatic membrane properties across species, we grouped human and mouse L5 neurons into physiologically defined cell types based on the same physiological features used in Figure 2 (Figure 7A-left). As previously explored with the human data (Figure 2), we then asked whether the physiologically defined cell types corresponded to genetically defined cell types via Patch-seq or labeling by a L5 ET neuron specific enhancer virus (Graybuck et al., 2021). Like clustering human data alone, clustering data from both species revealed at least three distinct types of neurons. For both species, physiologically defined L5 ET neurons corresponded to genetically defined L5 ET neurons (Figure 7A-right). Furthermore, L5 ET-like neurons in both species occupied similar areas of the tSNE plot of physiological features (Figure 7A). These data suggest that the intrinsic membrane properties of L5 ET neurons are broadly conserved in mouse and human neocortex.

Nonetheless, these observations do not exclude the possibility of subtler cross-species differences in the somatic membrane properties of L5 ET neurons. Thus, we also made pairwise comparisons between the somatic membrane properties of mouse and human neurons. For this analysis, we collapsed the two IT neuron types into one IT neuron group. We observed both cell type and cross-species differences in nearly every membrane property examined (Figure 7; Figure S7). To determine whether differences are larger between species or between cell types we calculated the effect size associated with each physiological feature. The cell-type-specific effect size was nearly always larger than the

effect size determined across species, with a few notable exceptions. For example, cross-species differences were larger than cross-cell-type differences for some suprathreshold properties, including input/output gain and action potential half-width (Figure 7; Figure S7).

Discussion

Investigation of the distinctive properties of L5 ET neurons in the human neocortex has been hampered by an inability to identify these neurons by their defining feature - subcerebral projection targets. In this study, we circumvent this problem by leveraging transcriptomic definitions of cell types, alignment of homologous cell types between mouse and human neocortical taxonomies, and Patch-seq mapping of human L5 neurons to the reference taxonomy to pin the identity of recorded cell types. We demonstrate that the morpho-electric properties and gene expression profiles in human L5 ET neurons are as distinctive as their rodent counterparts, highlighting a general conservation of the core defining features of L5 ET and L5 IT neurons. Additionally, our results reveal substantial divergence and specialization of cellular features along with a dramatic overall reduction in the abundance of the L5 ET type in primate versus rodent temporal cortex.

Patch-seq/patch-clamp recordings revealed broad morpho-electric similarities between rodent and human L5 ET neurons. In both rodent and human L5 ET neurons, HCN-channel-related membrane properties were enhanced compared with L5 IT neurons. In rodents, HCN-channel expression is enriched in the apical dendrite of L5 ET neurons, where it strongly shapes synaptic integration by narrowing the window whereby inputs can be summed in time (Dembrow et al., 2015; Harnett et al., 2015; Kalmbach et al., 2013, 2015, 2017; Williams and Stuart, 2000). These properties tend to make L5 ET neurons most sensitive to inputs containing frequency components in the theta band (4–12 Hz). Our findings indicate that many of these subthreshold integrative properties are conserved in human L5 ET neurons. We found that the distinguishing morphological feature of human L5 ET neurons, like their rodent counterparts, was a prominent apical tuft terminating in L1. This contrasts with neighboring human L5 IT neurons, which we observed to taper to a fine process terminating without forming an apical tuft. These observations are consistent with previous morphological reconstructions of infragranular spiny neurons in human temporal cortex (Mohan et al., 2015), which found that L5 pyramidal neuron apical dendrites usually end short of L1 without forming a tuft. Many rodent L5 IT neurons have a thin apical tuft, whereas others are tuftless like the human L5 IT neurons reported here (Larkman and Mason, 1990; Tantirigama et al., 2014). While a more thorough examination of diversity of human L5 neuron morphology across neocortical areas may uncover thin tufted L5 IT neurons, the differences in dendritic morphology we report here suggest that human L5 ET and IT neurons receive different types of synaptic input. The prominent apical tuft in L1 of human L5 ET neurons implies these neurons receive substantial feedback input from higher cortical areas and second order thalamic nuclei (Cauller et al., 1998; Rubio-Garrido et al., 2009).

In rodents, dendritic plateau potentials serve as a mechanism for associating bottom-up input arriving at the basal dendrites with top-down input arriving at the apical tuft in L1 (Larkum, 2013). Plateau potentials in rodents are associated with a burst of action potentials at the

soma in response to near-threshold current injections, which we also observed in human L5 ET neurons (Larkum et al., 1999; Shai et al., 2015). Using direct dendritic patch-clamp recordings, we showed that plateau potentials can be elicited in human L5 ET neuron dendrites, and that these events were strongly reminiscent of Ca^{2+} spikes in some rodent L5 ET neurons. Although we cannot rule of the possibility that some of our recordings could have been from L5 IT neuron dendrites, it remains to be seen whether human L5 IT dendrites similarly display electrogenesis. Nonetheless, L5 ET neurons in the human neocortex may perform a similar computation as rodent L5 ET neurons of coupling feedback and feedforward input in the neocortical circuit.

Our findings confirm some observations from the sole previous report of human L5 dendritic membrane properties (Beaulieu-Laroche et al., 2018), but we also note some key differences. As previously described, HCN-dependent membrane properties varied as a function of distance from the soma, except for input resistance. The flattened somatic-dendritic gradient of input resistance is a clear departure from rodent ET neurons (Kalmbach et al., 2013) and may reflect a relative decrease in the density of resting conductance in human L5 neurons (Beaulieu-Laroche et al., 2018). Unlike (Beaulieu-Laroche et al., 2018), we observed strong electrogenesis in human L5 ET dendrites, although we cannot comment on whether these spikes propagated to the soma. Notably, in the previous report dendritic recordings were made up to ~1.9 mm from the soma. As such, it is possible that locations distal to our recording sites (maximum ~1.1 mm) do not show strong electrogenesis. It is unlikely that differences in the underlying medical conditions of patient populations contributed to different findings as we observed dendritic plateau potentials in tissue derived from both epilepsy and tumor patients. Aside from methodological differences (external/internal solutions, slice preparation, surgical sampling etc.), there are several possible explanations for this discrepancy. In rodents, there is variability in the types of nonlinearities observed in L5 dendrites. For example, L5 ET neuron dendrites in the prefrontal cortex display strong Na^{+} mediated spikes but not Ca^{2+} plateaus, whereas in sensory cortical areas Ca^{2+} electrogenesis is ubiquitous (Gulledge and Stuart, 2003; Harnett et al., 2013; Kalmbach et al., 2017; Larkum et al., 1999; Santello and Nevian, 2015; Shai et al., 2015). Even within a single brain region, there are differences in the propensity of the apical trunk of L5 neurons to generate plateau potentials. Some of this variability appears to be related to differences in dendritic architecture (Fletcher and Williams, 2019). Similar variability in dendritic morphology and related electrogenesis may therefore occur in human neocortex. Nonetheless, our observations demonstrate that at least some human L5 ET neuron dendrites do in fact display strong dendritic electrogenesis.

While rodent and human L5 ET neurons had broadly similar genetic and morpho-electric properties, there were nonetheless many species differences that point to potential areas of cross-species divergence or specialization. Foremost among these was the striking sparsification of transcriptomically-defined L5 ET neurons in temporal cortex from mouse to macaque to human. A similar sparsification has been observed in primary motor cortex and frontoinsular cortex (Bakken et al. 2020; Hodge et al. 2020), brain regions with a greater abundance of L5 ET neurons compared with temporal cortex. In the prior studies and in the current study it was not feasible to directly demonstrate the extratelencephalic projections of these transcriptomically identified L5 neurons in the human brain. However,

homology mapping to identified L5 ET neurons in mouse provides strong inferential, albeit indirect, evidence of subcerebral axonal projections (e.g., Tasic et al., 2018). Furthermore, it remains possible there are additional subpopulations of L5 neurons in human temporal cortex that project to subcerebral areas but that were not captured by the specific genetic markers we evaluated in this study. Future efforts to perform homology mapping using non-human primate species, where techniques like retrograde labeling are feasible, may provide additional evidence to strengthen this claim. Nonetheless, the dearth of human L5 ET neurons we observed is consistent with previous observations and may reflect the dramatic increase in cortical volume relative to that of subcerebral projection targets in primates and humans (Heffner and Masterton, 1975; Herculano-Houzel et al., 2015). While it remains a possibility the method of quantification employed in our study detected a subset of all L5 ET neurons in temporal cortex region, our findings establish a relative abundance of this important cell type in mouse, macaque and human.

In addition to the cross-species differences that we observed, there are undoubtedly other differences that were not accessible to the methods used in this study. Chief among these is the somato-dendritic distribution of ion channels. Previous reports have shown that the human L5 dendrites are more electrically compartmentalized compared with rat dendrites (Beaulieu-Laroche et al., 2018), because of cross-species differences in the density of ion channels. Additionally, in the supragranular layers, human pyramidal neurons possess dendritic non-linearities not previously observed in rodent neurons (Gidon et al., 2020) that may be due to differences in the somato-dendritic expression of select ion channels. Furthermore, there could be differences in the passive membrane properties of human L5 ET neurons, or in related dendritic morphological properties (Deitcher et al., 2017; Eyal et al., 2016).

Finally, our general strategy of investigating L5 ET neurons could serve as a roadmap for studying human and non-human primate L5 ET neuron types across cortical areas. The transcriptomes of L5 ET neurons vary greatly across cortical areas in both rodents and humans (Hodge et al., 2020; Tasic et al., 2018), suggesting that areal signatures in functional properties may also greatly vary as a direct consequence. We recently utilized a similar approach to highlight conserved and divergent features of primate Betz cells and mouse corticospinal neurons (Bakken et al., 2020). Determining how cross-areal and cross-species variability in gene expression translates to phenotypic diversity at the level of cell types promises to deepen our understanding of conserved and divergent aspects of neocortical brain function through evolution and to improve prospects for translational neuroscience.

STAR Methods

RESOURCE AVAILABILITY

Lead Contact—Further information and requests for resources and reagents should be directed to and will be fulfilled by the lead contact, Brian Kalmbach (briank@alleninstitute.org)

Materials Availability—This study did not generate new unique reagents.

Data and Code Availability—Raw single-cell RNA-seq data from patch-seq experiments will be deposited at dbGAP. In addition, gene counts from patch-seq samples have been deposited at https://portal.brain-map.org/explore/classes/multimodal-characterization/human-l5-et-it and are publicly available as of the date of publication. These identifiers are also listed in the key resources table. SWC files from morphological reconstructions have been deposited at Brain Image Library and are publicly available at the time of publication. Identifiers are listed in the key resource table. Physiology data and mFISH data reported in this paper will be shared by the lead contact upon request.

Analysis code has been deposited at Zenodo and is publicly available as of the date of publication. DOIs are listed in the key resources table.

Any additional information required to reanalyze the data reported in this paper is available from the Lead Contract upon request.

EXPERIMENTAL MODEL AND SUBJECT DETAILS

Human surgical specimens.—Surgical specimens were obtained from local hospitals (University of Washington Medical Center, Swedish Medical Center and Harborview Medical Center). Hospital institute review boards approved all procedures involving human tissue before commencing the study and all patients provided informed consent. Data included in this study were obtained from neurosurgical tissue resections for the treatment of refractory temporal lobe epilepsy (n=23) or deep brain tumors (n=5) in 22 male and 6 female patients with a mean age of 40.4 ± 3.1 years (Table S4). We did not detect any influence of sex/gender on the physiological/transcriptomic classification of cell types.

Mouse specimens.—All procedures involving mice were approved by the Allen Institute's Institutional Care and Use Committee. Mixed strains of male and female transgenic mice (Thy1-eyfp (B6.Cg-Tg(Thy1-YFP)-HJrs/J, C57BL/6-Tg (Pvalb-tdTomato)15Gfng/J) from 60–90 days old were used for experiments. Mice were maintained on a 12-hour light/dark cycle in a temperature and humidity controlled room. Mice were housed 3–5 per cage with free access to food and water. We did not detect any influence of sex on the physiological/transcriptomic classification of cell types.

Macaque specimens.—All procedures involving macaque monkeys were approved by the University of Washington's Institutional Care and Use Committee. Male (n=2) and female (n=1) macaques (macaca nemestrina) from 3–17 years old designated for use in the Washington National Primate Research Center's Tissue Distribution Program were used for experiments. Monkeys were housed in individual cages on a 12-hour light/dark cycle in a temperature and humidity controlled room. There was no obvious influence of sex on the relative distribution of L5 neurons positive for L5 ET markers in mFISH experiments.

METHOD DETAILS

Acute brain slice preparation.—Brain slice preparation was similar for all species. Human neurosurgical specimens deemed not to be of diagnostic value were placed in a sterile, prechilled, carbogenated (95% O_2/5% CO_2) container filled with an artificial

cerebrospinal fluid composed of (in mM): 92 N-methyl-D-glucamine (NMDG), 2.5 KCl, 1.25 NaH_2PO_4, 30 $NaHCO_3$, 20 4-(2-hydroxyethyl)-1-piperazineethanesulfonic acid (HEPES), 25 glucose, 2 thiourea, 5 Na-ascorbate, 3 Na-pyruvate, 0.5 $CaCl_2 \cdot 4H_2O$ and 10 $MgSO_4 \cdot 7H_2O$. Surgical specimens were quickly transported from the surgical site to the Institute while continuously bubbled with carbogen. Macaques were anesthetized with sevoflurane gas during which the entire cerebrum was extracted and placed in the same aCSF described above. After brain extraction, monkeys were administered intravenous injection of a lethal dose of sodium-pentobarbital. We then dissected the superior temporal gyrus of the temporal lobe for brain slice preparation. Mice were deeply anesthetized by intraperitoneal administration of Avertin (20 mg/kg) and were perfused through the heart with the same NMDG aCSF described above.

Brain specimens were sectioned on a Compresstome VF-200 using a zirconium ceramic blade (Precisionary Instruments) at 300 or 350 μm using the protective recovery method (Ting et al., 2014). To ensure that the dendrites of pyramidal neurons were relatively intact, human specimens were trimmed and mounted such that the angle of slicing was perpendicular to the pial surface. Mouse brains were sectioned in the coronal plane.

Patch clamp recordings.—Brain slices were placed in a submerged, heated recording chamber that was continuously perfused with carbogenated aCSF consisting of (in mM): 119 NaCl, 2.5 KCl, 1.25 NaH2PO4, 24 NaHCO3, 12.5 glucose, 2 CaCl2·4H2O and 2 MgSO4·7H2O (pH 7.3–7.4). Slices were visualized with an Olympus BX51WI microscope and infrared differential interference contrast (IR-DIC) optics and a 40x water immersion objective.

Patch pipettes (2–5 MΩ for somatic; 4–8 MΩ for dendritic) were filled with one of two internal solutions. The first solution contained (in mM): 126.0 K-gluconate, 10.0 HEPES, 0.3 EGTA, 4.0 mM KCl, 4 Mg-ATP, 0.3 Na2-GTP, 10.0 phosphocreatine disodium salt hydrate, 0.5% biocytin and .02 Alexa 594 or 488. The second pipette solution was used for Patch-seq experiments and contained (in mM): 110.0 K-gluconate, 10.0 HEPES, 0.2 EGTA, 4 KCl, 0.3 Na2-GTP, 10 phosphocreatine disodium salt hydrate, 1 Mg-ATP, 20 μg/ml glycogen, 0.5U/μL RNAse inhibitor (Takara, 2313A), 0.5% biocytin and 0.02 Alexa 594 or 488. The pH of both solutions was adjusted to 7.3 with KOH. Alexa filled neurons were visualized upon termination of recording using a 540/605 nm excitation/emission filter set. The liquid junction potential was calculated to be −13 mV and was not corrected.

Whole cell somatic and dendritic recordings were acquired using a Multiclamp 700B amplifier and either PClamp 10 data acquisition software or custom MIES acquisition software (https://github.com/AllenInstitute/MIES/) written in Igor Pro. Electrical signals were digitized at 20–50 kHz by an Axon Digidata 1550B (Molecular Devices) or an ITC-18 (HEKA) and were filtered at 2–10 kHz. Upon attaining whole cell current clamp mode, the pipette capacitance was compensated and the bridge was balanced. Access resistance was monitored throughout the recording and was 8–30 MΩ for somatic recordings and 15–40 MΩ for dendritic recordings.

Processing of Patch-seq samples.—Patch seq samples were processed as previously described (Lee et al., 2020). Prior to data collection for these experiments, all surfaces were thoroughly cleaned with RNAse Zap, and as needed DNAse Away. At the end of Patch-seq recordings, negative pressure (~−20 mbar) was applied through the pipette for ~5 minutes after which the nucleus was extracted by very slow pipette withdrawal with higher negative pressure (~−70 to −100 mbar). The pipette was removed from the recording chamber and the contents of the pipette were expelled into a PCR tube containing lysis buffer (Takara, 634894). Patch-seq sample tubes were held on dry ice in a benchtop plexiglass enclosure throughout the recording session to ensure collected samples remained free of RNAse and DNAse contamination. Sample tubes were then transferred to −80C for storage until further processing. cDNA libraries were produced using the SMART-Seq v4 Ultra Low Input RNA Kit for Sequencing (Takara 634894, Lot 1709695A) according to the manufacturer's instructions, using 20 PCR cycles for cDNA amplification. Samples proceeded through library construction using Nextera XT DNA Library Preparation Kit (Illumina FC-131–1096) according to the manufacturer's instructions except at 0.2x reaction size. Samples were sequenced to approximately 1million paired-end 50b reads//sample.

Biocytin histology.—As described previously (Gouwens et al., 2019), a horseradish peroxidase (HRP) enzyme reaction using diaminobenzidine (DAB) as the chromogen was used to visualize biocytin-filled neurons following physiological recordings. 4,6-diamidino-2-phenylindole (DAPI) stain was also used to identify cortical layers.

Slices were mounted and imaged on an upright AxioImager Z2 microscope (Zeiss, Germany) equipped with an Axiocam 506 monochrome camera and 0.63x optivar. High-resolution image stacks were captured with a 63X objective at 0.44 µm increments along the Z axis. ZEN software was used to stitch tiled images.

For a subset (n=28 human n=12 mouse) of the patch-clamp neurons, we measured the depth of somata from the pial surface of the brain in DAB/DAPI processed brain slices. For human patch clamp recordings, L5 ET (range 1594–2024, mean 1802.6 ± 50.5 µm) and L5 IT neurons (range 1460–2148, mean 1805 ± 45.3 µm) were sampled at similar depths from the pia. Mouse neurons were localized to layer 5 (range 407–814, mean 643.33 ± 36.9 µm). Recorded human L5 ET neurons suitable for morphological reconstruction in this study were concentrated in the upper portion of L5 (relative depth within L5 – range 0.13–0.45, mean 0.28 ± 0.04). The location of these recordings is consistent with observations that *POU3F1* (relative depth within L5 – range 0.06–0.72, mean 0.36 ± 0.02) and *FAM84B* (relative depth within L5 – 0.01–0.91, mean 0.33 ± 0.04) positive neurons are enriched in the superficial portion of L5 (Figures 1, S1 and S2).

Additionally, images of the DAPI stain were used to confirm that somata were localized to L5.

Multiplex fluorescence in situ hybridization.—Fresh-frozen human (postmortem and surgical) MTG, macaque (*Macaca nemestrina)* temporal cortex, and mouse TEa tissues were sectioned at 14–16 µm onto Superfrost Plus glass slides (Fisher Scientific). Sections were prepared from at least two donors per species. Sections were dried for 20 minutes at −20°C

and then vacuum sealed and stored at −80°C until use. The RNAscope multiplex fluorescent v1 kit was used per the manufacturer's instructions for fresh-frozen tissue sections (ACD Bio), except that fixation was performed for 60 minutes in 4% paraformaldehyde in 1X PBS at 4°C, post-dehydration drying was done for 15 minutes at 37°C and protease treatment was shortened to 10 minutes. Sections were imaged using a 60X oil immersion lens on a Nikon TiE fluorescence microscope equipped with NIS-Elements Advanced Research imaging software (version 4.20). For all RNAscope mFISH experiments, positive cells were called by manually counting RNA spots for each gene. Cells were called positive for a gene if they contained ≥3 RNA spots for that gene. SLC17A7 provided a boundary for excitatory cell bodies and helped to determine which spots were localized to cell bodies. Some dots were not closly associated with cell bodies and were likely transcripts associated with processes that weren't otherwise visible in the image (e.g. Figure S1). Lipofuscin autofluorescence was distinguished from RNA spot signal based on the larger size of lipofuscin granules and broad fluorescence spectrum of lipofuscin.

To quantify the fraction of ET cells (defined as *FAM84B* and *SLC17A7* double positive cells or alternatively, *POU3F1* and *SLC17A7* double positive cells) in L5 in each species, the boundary of L5 was first delineated using DAPI to identify cortical layers. The total number of *SLC17A7*+ cells within layer 5 was quantified and then the total number of *SLC17A7*+,*FAM84B*+ cells (or *SLC17A7*+, *POU3F1*+ cells) in layer 5 was quantified. The percentage of putative L5 ET cells (*SLC17A7*+, *FAM84B*+) was then calculated as a fraction of the total number of *SLC17A7*+ cells in L5. Counts were repeated on at least 2 donors per species and at least 2 sections per donor. Marker genes were selected by identifying L5 ET neuron enriched genes (relative to all other excitatory types) in both mouse and human sc/snRNA-seq datasets (Figure S1A and S1B; Hodge et al., 2019; Tasic et al., 2018; https://portal.brain-map.org/explore/transcriptome).

QUANTIFICATION AND STATISTICAL ANALYSIS

Neurophysiology.—We used three basic current stimuli to probe the intrinsic membrane properties of L5 neurons. In the first protocol, we measured the voltage response to a series of 1s steps from −150 pA to +50 pA in +20 pA increments. Maximum and steady-state input resistance (R_N) were calculated from the linear portion of the current-maximum or steady state voltage relationship generated in response to these current injections. Voltage sag was defined as the ratio of maximum to steady-state R_N. Rebound slope was calculated from the slope of the rebound amplitude as a function of steady-state membrane potential.

The second stimulus was a chirp stimulus that increased in frequency either linearly from 1–15 Hz over 15 s or logarithmically from 0.2–40 Hz over 20s. The amplitude of the chirp was adjusted for each neuron to produce a peak-to-peak voltage deflection of ~10 mV. Impedance amplitude (ZAP) was derived as the ratio of the Fourier transform of the voltage response to the Fourier transform of the chirp: $|Z(f| = \sqrt{\mathrm{Re}(Z(f))^2 + (Im(Z(f))^2}$, where Im(Z(f)) and Re(Z(f)) are the imaginary and real parts of the impedance Z(f), respectively. The frequency at which the maximum impedance occurred was the resonant frequency (f_R). Resonance strength (Q) was measured as the ratio of the maximum impedance amplitude to the impedance amplitude at 1 Hz. The 3dB cutoff was defined as the frequency at which

the ZAP profile attenuated to a value of $\sqrt{(1/2)Zmax}$. Impedance phase (ZPP) was derived as: $\phi(f) = tan^{-1}\frac{Im(Z(f))}{(Re(Z(f))}$. Total inductive phase (ZΦ) was defined as the area under the inductive part of the ZPP. Synchrony phase was the frequency at which the ZPP was 0. ZPP and ZAP plots were smoothed using a running median smooting function.

The third stimulus was a series of 1 second depolarizing current injections increasing in amplitude by +50 pA/step. We measured the number of spikes and the first instantaneous firing rate in response to each current injection. Gain was defined as the linear slope of this action potential frequency-current relationship. Single action potential properties were measured from voltage responses to the lowest current that produced a spike. Action potential threshold was defined as the voltage at which the first derivative of the voltage response exceeded 20 V/s. AP width was measured at half the amplitude between threshold and the peak voltage. Fast AHP was defined relative to threshold. Spike frequency accommodation (SFA) and medium afterhyperpolarization (mAHP) were calculated from current injections producing ~10 spikes during the 1 s step. SFA was defined as the ratio of the second to the last interspike interval. The mAHP was defined as the minimum voltage after the spike train. For dendritic recordings we also quantified the area and width of plateau potentials. The threshold for a plateau was defined as the voltage where the first derivative reached 2 V/s. Plateau width at half maximum amplitude and plateau area were calculated relative to this threshold.

We grouped neurons based on physiological properties derived from these current injections using hierarchical clustering. First we performed principal component analysis on all physiological features. Principal components explaining at least 1% of the variance were then used to cluster neurons into groups using Ward's algorithm. The number of clusters was determined using the sigClust package in R which generates a p value for the null hypothesis that data points are drawn from a single Gaussian as opposed to two Gaussian distributions. The p value for this analysis was set at < 0.01, which yielded three clusters.

Random forest classifiers were constructed using the randomForest package in R (Liaw and Wiener, 2002). We varied the percentage of cells included in the training data set from 10–50%. For each training set, we constructed 100 forests consisting of 100 trees. Mean accuracy and importance values were calculated from each set of forests on the data held out of the training sets.

Comparisons across groups are presented as geometric box plots unless otherwise denoted. The exact value of n can be found in the text, figures or legends and represents number of cells. Statistical significance was assayed using ANOVAs, t-tests, Mann-Whitney U tests, or Person's correlation where appropriate. P values were FDR adjusted for multiple comparisons. Effect sizes are reported as eta-squared values. Statistical analysis was performed in R.

Morphological reconstruction.—Dendritic reconstructions were generated based on a digital 3D image stack that was run through a Vaa3D-based image processing and reconstruction pipeline, as previously described (Gouwens et al., 2019). A full list of pairwise feature comparison can be found in Table S3. Somatic morphology was quantified

directly via a maximum projection of a series of 63x images of biocytin and DAB reacted neurons. The initial apical shaft width was measured 50 μm from the center of the soma. The exact value of n can be found in the text, figures or supplemental tables and represents number of cells.

Patch-Seq sample mapping.—To determine the corresponding transcriptomic cell type for each Patch-seq sample, we utilized a tree-based mapping strategy (Gouwens et al., 2020). For each neuron, we computed its correlation with each branch of the reference cell type taxonomy, starting from the root and working towards the leaves. Marker genes associated with each branch of the taxonomy were used for correlations. The confidence of the mapping was determined by applying 100 bootstrapping iterations of the process. For each iteration 70% of the reference cells and 70% of maker genes were randomly sampled for mapping. The percentage of times a given cell mapped to a given transcriptomic cell types was the mapping probability. Only neurons with a mapping probability greater than 50% to a given terminal leaf were included. As an additional quality control measure, only Patch-seq samples with a normalized summed expression of “on”-type marker genes (NMS; (Tripathy et al., 2018) were included. We mapped mouse Patch-seq samples to a published mouse VISp scRNA-seq cell type taxonomy (Tasic et al., 2018) and human samples to a published human MTG snRNA-seq cell type taxonomy (Hodge et al., 2019).

Differential Gene Expression analysis.—To identify differentially expressed genes between L5 ET and L5 IT neurons for each species, expression matrices were trimmed to only include genes with one-to-one orthologs in human and mouse (downloaded from NCBI Homologene in November, 2019). Comparisons across species are complicated by the lack of a clear rodent homologue to human MTG and by evidence that L5 ET neuron gene expression varies greatly between cortical areas in the human and mouse (Hodge et al., 2019; Tasic et al., 2018). Rather than focusing on a single mouse brain region, we utilized a published scRNA-seq dataset derived from two brain regions, the mouse primary visual cortex (VISp) and the anterior lateral motor cortex (ALM; Tasic et al. 2018).Raw expression matrices for each brain region were CPM normalized then Log2 transformed. Average expression was determined for each subclass (i.e. L5 ET and L5 IT), then log fold change was determined between subclasses for each brain region. The following clusters from human MTG (Hodge et al., 2019) were used for L5 IT subclass input; Exc L5–6 RORB TTC12, Exc L4–5 RORB FOLH1B, Exc L5–6 THEMIS C1QL3, Exc L4–6 RORB SEMA3E, and Exc L4–6 RORB C1R; and the Exc L4–5 FEZF2 SCN4B cluster was used as input for L5 ET. For mouse, all previously defined VISp and ALM L5 IT and L5 PT (which is another common name for L5 ET) clusters defined in Tasic et al., 2018 were used as input. Initial GO analysis of conserved L5 ET DE genes (> 0.5 Log2FC across all three brain regions) with PANTHER Classification System (Mi et al., 2019) revealed numerous significant GO biological process categories for axonogenesis, axon guidance, axon development, etc. Additionally, numerous synapse-related categories were enriched (i.e synaptic membrane adhesion, synaptic organization, synaptic structure, etc.). Respective terms were aggregated into an Axon Guidance gene list, and a Synaptic Regulation gene list for visualization purposes in Figure 1. Human L5 ET-enriched (> 1 Log2FC) DE genes from each GO category were plotted as line plots and colored red if L5 ET neurons had > 1

Log2FC expression over L5 IT in all brain regions, indicating conserved L5 ET DE genes. Lines were colored blue if L5 ET expression was > 1 Log2FC in human MTG and < 0 in both mouse regions, indicating human-specific L5 ET DE genes.

Supplementary Material

Refer to Web version on PubMed Central for supplementary material.

Acknowledgments

We wish to thank the Allen Institute founder, Paul G. Allen, for his vision, encouragement and support. We also thank Luke Esposito, Julie Nyhus and the Tissue Procurement team, Tamara Casper, Eliza Barkan, Matthew Kroll, Herman Tung, Josef Sulc and Kirsten Crichton of the Tissue Processing Team, and the Facilities team for help in coordinating the logistics of human surgical tissue collection, transport and processing. We thank collaborators at the local hospital sites, including Caryl Tongco, Jae-Guen Yoon, Nathan Hansen, Gina DeNoble and Allison Beller, Erica Melief, Lisa Keene, Desiree Marshall, and Caitlin Latimer for assistance with various logistics. We thank Ximena Opitz-Araya, Miranda Walker and Tae Kyung Kim for molecular cloning and packaging of AAV vectors, and Ali Cetin, Shenqin Yao, Marty Mortrud, and Thomas Zhou of the Viral Technology team for AAV packaging. We thank Peter Chong for reagent prep and assistance with tissue processing. We thank Krissy Brouner, Augustin Ruiz, Tom Egdorf, Amanda Gary, Michelle Maxwell, Alice Pom and Jasmine Bomben of the Histology team for biocytin staining. We thank Nadezhda Dotson, Rachel Enstrom, Madie Hupp, Lydia Potekhina, Kiet Ngo, Samuel Dingman Lee, Melissa Gorham, Fiona Griffin, Eric Lee, and Shea Ransford of the Imaging team for imaging of biocytin filled cells. We thank Darren Bertagnolli, Michael Tieu, Delissa McMillen, Thanh Pham, Christine Rimorin, Katelyn Ward, Alexandra Glandon, and Amy Torkelson of the RSeq core for scRNA-seq processing. We thank Jeremy A. Miller, Osnat Penn, and Zizhen Yao for contributions to the Patch-seq tree-based mapping algorithms, and Jeff Goldy and Olivia Fong for Patch-seq data management and updates in MolGen Shiny. We thank Jim Berg, Lindsay Ng, Rusty Mann, Jessica Trinh and other members of the Ephys Core for assistance with sample processing and reporting. We thank the Animal Care Team for mouse husbandry, the Allen Institute Transgenic Colony Management team for colony management, the Allen Institute Laboratory Animal Services team for preparation and delivery of experimental mice. We thank Mia Kalmbach making the illustrations in the graphical abstract. We thank Abi Gibson for help with morphological reconstructions. We thank the Allen Institute *in vitro* single cell characterization project team and the Mouse and Human Transcriptomics project teams for their guidance in this work.

This work was funded by the Allen Institute for Brain Science and also supported in part by the U.S. National Institutes of Health (NIH) grant U01 MH114812–02 to E.S.L., NIH BRAIN Initiative award RF1MH114126 from the National Institute of Mental Health to E.S.L., J.T.T., and B.P.L., NIH BRAIN Initiative RF1MH121274 and NIH R01DA036909 awards to B.T. NIA grant AG005136 to the UW ADRC Neuropathology Core, a grant from the Nancy and Buster Alvord Endowment to C.D.K., and NIH grants P51OD010425 from the Office of Research Infrastructure Programs (ORIP) and UL1TR000423 from the National Center for Advancing Translational Sciences (NCATS). Its contents are solely the responsibility of the authors and do not necessarily represent the official view of NIH, ORIP, NCATS, the Institute of Translational Health Sciences or the University of Washington National Primate Research Center.

References

Allman JM, Tetreault NA, Hakeem AY, Manaye KF, Semendeferi K, Erwin JM, Park S, Goubert V, and Hof PR (2010). The von Economo neurons in frontoinsular and anterior cingulate cortex in great apes and humans. Brain Struct. Funct 214, 495–517. [PubMed: 20512377]

Anastasiades PG, Marlin JJ, and Carter AG (2018). Cell-Type Specificity of Callosally Evoked Excitation and Feedforward Inhibition in the Prefrontal Cortex. CellReports 22, 679–692.

Arlotta P, Molyneaux BJ, Chen J, Inoue J, Kominami R, and Macklis JD (2005). Neuronal Subtype-Specific Genes that Control Corticospinal Motor Neuron Development In Vivo. Neuron 45, 207–221. [PubMed: 15664173]

Avesar D, and Gulledge AT (2012). Selective serotonergic excitation of callosal projection neurons. Front. Neural Circuits 6, 1–11. [PubMed: 22291618]

Baker A, Kalmbach B, Morishima M, Kim J, Juavinett A, Li N, and Dembrow N (2018). Specialized Subpopulations of Deep-Layer Pyramidal Neurons in the Neocortex: Bridging Cellular Properties to Functional Consequences. J. Neurosci 118–150.

Bakken TE, Jorstad NL, Hu Q, Lake BB, Tian W, Kalmbach BE, Crow M Hodge RD, Krienen FM, Sorensen SA, Eggermont J, Yao Z, Aevermann D, Aldridge AI, et al. Evolution of cellular diversity in primary motor cortex of human, marmoset monkey, and mouse. BioRxiv 116. 10.1101/2020.03.31.016972

Beaulieu-Laroche L, Toloza EHS, van der Goes M-S, Lafourcade M, Barnagian D, Williams ZM, Eskandar EN, Frosch MP, Cash SS, and Harnett MT (2018). Enhanced Dendritic Compartmentalization in Human Cortical Neurons. Cell 175, 643–651.e14. [PubMed: 30340039]

Berg J, Sorensen SA, Ting JT, Miller JA, Chartrand T, Buchin A, Bakken TE, Budzillo A, Dee N, Ding S-L, et al. (2020). Human cortical expansion involves diversification and specialization of supragranular intratelencephalic-projecting neurons. BioRxiv 10.1101/2020.03.31.018820.

Brown SP, and Hestrin S (2009). Intracortical circuits of pyramidal neurons reflect their long-range axonal targets. Nature 457, 1133–1136. [PubMed: 19151698]

Cauller LJ, Clancy B, and Connors BW (1998). Backward cortical projections to primary somatosensory cortex in rats extend long horizontal axons in layer I. J. Comp. Neurol 390, 297–310. [PubMed: 9453672]

Deitcher Y, Eyal G, Kanari L, Verhoog MB, Atenekeng Kahou GA, Mansvelder HD, de Kock CPJ, and Segev I (2017). Comprehensive Morpho-Electrotonic Analysis Shows 2 Distinct Classes of L2 and L3 Pyramidal Neurons in Human Temporal Cortex. Cereb. Cortex 1–17. [PubMed: 28365777]

Dembrow N, and Johnston D (2014). Subcircuit-specific neuromodulation in the prefrontal cortex. Front. Neural Circuits 8, 54–54. [PubMed: 24926234]

Dembrow NC, Chitwood RA, and Johnston D (2010). Projection-specific neuromodulation of medial prefrontal cortex neurons. J. Neurosci 30, 16922–16937. [PubMed: 21159963]

Dembrow NC, Zemelman BV, and Johnston D (2015). Temporal dynamics of L5 dendrites in medial prefrontal cortex regulate integration versus coincidence detection of afferent inputs. J. Neurosci 35, 4501–4514. [PubMed: 25788669]

Economo MN, Viswanathan S, Tasic B, Bas E, Winnubst J, Menon V, Graybuck LT, Nguyen TN, Smith KA, Yao Z, et al. (2018). Distinct descending motor cortex pathways and their roles in movement. Nature 563, 79–84. [PubMed: 30382200]

Eyal G, Verhoog MB, Testa-Silva G, Deitcher Y, Lodder JC, Benavides-Piccione R, Morales J, DeFelipe J, de Kock CP, Mansvelder HD, et al. (2016). Unique membrane properties and enhanced signal processing in human neocortical neurons. ELife 5.

Fletcher LN, and Williams SR (2019). Neocortical Topology Governs the Dendritic Integrative Capacity of Layer 5 Pyramidal Neurons. Neuron 101, 76–90.e4. [PubMed: 30472076]

Gao WJ, and Zheng ZH (2004). Target-specific differences in somatodendritic morphology of layer V pyramidal neurons in rat motor cortex. J. Comp. Neurol. 476, 174–185. [PubMed: 15248197]

Gidon A, Zolnik TA, Fidzinski P, Bolduan F, Papoutsi A, Poirazi P, Holtkamp M, Vida I, and Larkum ME (2020). Dendritic action potentials and computation in human layer 2/3 cortical neurons. 87, 83–87.

Gouwens NW, Sorensen SA, Berg J, Lee C, Jarsky T, Ting J, Sunkin SM, Feng D, Anastassiou CA, Barkan E, et al. (2019). Classification of electrophysiological and morphological neuron types in the mouse visual cortex. Nat. Neurosci 22, 1182–1195. [PubMed: 31209381]

Gouwens NW, Sorensen SA, Baftizadeh F, Budzillo A, Lee BR, Jarsky T, Alfiler L, Baker K, Barkan E, Berry K, et al. (2020). Integrated Morphoelectric and Transcriptomic Classification of Cortical GABAergic Cells. Cell 183, 935–953.e19. [PubMed: 33186530]

Graybuck LT, Daigle TL, Sedeño-Cortés AE, Walker M, Kalmbach B, Lenz GH, Morin E, Nguyen TN, Garren E, Bendrick JL, et al. (2021). Enhancer viruses for combinatorial cell-subclass-specific labeling. Neuron S0896627321001598.

Groh A, Meyer HS, Schmidt EF, Heintz N, Sakmann B, and Krieger P (2010). Cell-Type Specific Properties of Pyramidal Neurons in Neocortex Underlying a Layout that Is Modifiable Depending on the Cortical Area. Cereb. Cortex 20, 826–836. [PubMed: 19643810]

Guan D, Armstrong WE, and Foehring RC (2015). Electrophysiological properties of genetically identified subtypes of layer 5 neocortical pyramidal neurons: Ca 2+dependence and differential modulation by norepinephrine. J. Neurophysiol 2014–2032. [PubMed: 25568159]

Gulledge AT, and Stuart GJ (2003). Action potential initiation and propagation in layer 5 pyramidal neurons of the rat prefrontal cortex: absence of dopamine modulation. J. Neurosci 23, 11363–11372. [PubMed: 14673000]

Harnett MT, Xu N-L, Magee JC, and Williams SR (2013). Potassium channels control the interaction between active dendritic integration compartments in layer 5 cortical pyramidal neurons. Neuron 79, 516–529. [PubMed: 23931999]

Harris KD, and Shepherd GMG (2015). The neocortical circuit: themes and variations. Nat. Neurosci 18, 170–181. [PubMed: 25622573]

Hattox AM, and Nelson SB (2007). Layer V Neurons in Mouse Cortex Projecting to Different Targets Have Distinct Physiological Properties. J. Neurophysiol 98, 3330–3340. [PubMed: 17898147]

Heffner R, and Masterton B (1975). Variation in Form of the Pyramidal Tract and Its Relationship to Digital Dexterity; pp. 175–187. Brain. Behav. Evol 12, 175–187.

Herculano-Houzel S, Catania K, Manger PR, and Kaas JH (2015). Mammalian Brains Are Made of These: A Dataset of the Numbers and Densities of Neuronal and Nonneuronal Cells in the Brain of Glires, Primates, Scandentia, Eulipotyphlans, Afrotherians and Artiodactyls, and Their Relationship with Body Mass. Brain. Behav. Evol 86, 145–163. [PubMed: 26418466]

Hodge RD, Bakken TE, Miller JA, Smith KA, Barkan ER, Graybuck LT, Close JL, Long B, Johansen N, Penn O, et al. (2019). Conserved cell types with divergent features in human versus mouse cortex. Nature 573, 61–68. [PubMed: 31435019]

Hodge RD, Miller JA, Novotny M, Kalmbach BE, Ting JT, Bakken TE, Aevermann BD, Barkan ER, Berkowitz-Cerasano ML, Cobbs C, et al. (2020). Transcriptomic evidence that von Economo neurons are regionally specialized extratelencephalic-projecting excitatory neurons. Nat. Commun 11, 1172–1172. [PubMed: 32127543]

Jacobs B, Garcia ME, Shea-Shumsky NB, Tennison ME, Schall M, Saviano MS, Tummino TA, Bull AJ, Driscoll LL, Raghanti MA, et al. (2017). Comparative morphology of gigantopyramidal neurons in primary motor cortex across mammals. J. Comp. Neurol 526, 496–536. [PubMed: 29088505]

Kalmbach BE, Chitwood RA, Dembrow NC, and Johnston D (2013). Dendritic generation of mGluR-mediated slow afterdepolarization in layer 5 neurons of prefrontal cortex. J. Neurosci 33, 13518–13532. [PubMed: 23946410]

Kalmbach BE, Johnston D, and Brager DH (2015). Cell-Type Specific Channelopathies in the Prefrontal Cortex of the fmr1-/y Mouse Model of Fragile X Syndrome(1,2,3). ENeuro 2.

Kalmbach BE, Gray R, Johnston D, and Cook EP (2017). Systems-based analysis of dendritic nonlinearities reveals temporal feature extraction in mouse L5 cortical neurons. J. Neurophysiol 117, 2188–2208. [PubMed: 28250154]

Kalmbach BE, Buchin A, Long B, Close J, Nandi A, Miller JA, Bakken TE, Hodge RD, Chong P, de Frates R, et al. (2018). h-Channels Contribute to Divergent Intrinsic Membrane Properties of Supragranular Pyramidal Neurons in Human versus Mouse Cerebral Cortex. Neuron 1–21.

Kawaguchi Y (2017). Pyramidal Cell Subtypes and Their Synaptic Connections in Layer 5 of Rat Frontal Cortex. Cereb. Cortex 27, 5755–5771. [PubMed: 29028949]

Kim EJ, Juavinett AL, Kyubwa EM, Jacobs MW, and Callaway EM (2015). Three Types of Cortical Layer 5 Neurons That Differ in Brain-wide Connectivity and Function. Neuron 88, 1253–1267. [PubMed: 26671462]

Larkman A, and Mason A (1990). Correlations between morphology and electrophysiology of pyramidal neurons in slices of rat visual cortex. I. Establishment of cell classes. J. Neurosci. Off. J. Soc. Neurosci 10, 1407–1414.

Larkum M (2013). A cellular mechanism for cortical associations: an organizing principle for the cerebral cortex. Trends Neurosci. 36, 141–151. [PubMed: 23273272]

Larkum ME, Zhu JJ, and Sakmann B (1999). A new cellular mechanism for coupling inputs arriving at different cortical layers. Nature 398, 338–341. [PubMed: 10192334]

Lee BR, Budzillo A, Hadley K, Miller JA, Jarsky T, Baker K, Hill D, Kim L, Mann R, Ng L, et al. (2021). Scaled, high fidelity electrophysiological, morphological, and transcriptomic cell characterization. eLife 10.7554/eLife.65482.

Li N, Chen T-W, Guo ZV, Gerfen CR, and Svoboda K (2015). A motor cortex circuit for motor planning and movement. Nature 1–16.

Liaw A, and Wiener M (2002). Classification and Regression by randomForest. R News 2, 18–22.

Mao T, Kusefoglu D, Hooks BM, Huber D, Petreanu L, and Svoboda K (2011). Long-Range Neuronal Circuits Underlying the Interaction between Sensory and Motor Cortex. Neuron 72, 111–123. [PubMed: 21982373]

Markram H, Muller E, Ramaswamy S, Reimann MW, Abdellah M, Sanchez CA, Ailamaki A, Alonso-Nanclares L, Antille N, Arsever S, et al. (2015). Reconstruction and Simulation of Neocortical Microcircuitry. Cell 163, 456–492. [PubMed: 26451489]

Mason A, and Larkman A (1990). Correlations between morphology and electrophysiology of pyramidal neurons in slices of rat visual cortex. II. Electrophysiology. J. Neurosci. Off. J. Soc. Neurosci 10, 1415–1428.

Mi H, Muruganujan A, Ebert D, Huang X, and Thomas PD (2019). PANTHER version 14: more genomes, a new PANTHER GO-slim and improvements in enrichment analysis tools. Nucleic Acids Res. 47, D419–D426. [PubMed: 30407594]

Mohan H, Verhoog MB, Doreswamy KK, Eyal G, Aardse R, Lodder BN, Goriounova NA, Asamoah B, B Brakspear ABC, Groot C, et al. (2015). Dendritic and Axonal Architecture of Individual Pyramidal Neurons across Layers of Adult Human Neocortex. Cereb. Cortex 25, 4839–4853. [PubMed: 26318661]

Oswald MJ, Tantirigama MLS, Sonntag I, Hughes SM, and Empson RM (2013). Diversity of layer 5 projection neurons in the mouse motor cortex. Front. Cell. Neurosci 7, 174–174. [PubMed: 24137110]

Otsuka T, and Kawaguchi Y (2008). Firing-Pattern-Dependent Specificity of Cortical Excitatory Feed-Forward Subnetworks. J. Neurosci. Off. J. Soc. Neurosci 28, 11186–11195.

Pathak D, Guan D, and Foehring RC (2016). Roles of specific Kv channel types in repolarization of the action potential in genetically identified subclasses of pyramidal neurons in mouse neocortex. J. Neurophysiol 115, 2317–2329. [PubMed: 26864770]

R Core Team (2018). R: A language and environment for statistical computing (R Foundation for Statistical Computing). https://www.R-project.org/.

Ramaswamy S, and Markram H (2015). Anatomy and physiology of the thick-tufted layer 5 pyramidal neuron. Front. Cell. Neurosci 9.

Robinson RB, and Siegelbaum SA (2003). Hyperpolarization-activated cationic currens: From Molecules to Physiological Function. Annu. Rev. Physiol 65, 453–480. [PubMed: 12471170]

Rojas-Piloni G, Guest JM, Egger R, Johnson AS, Sakmann B, and Oberlaender M (2017). Relationships between structure, in vivo function and long-range axonal target of cortical pyramidal tract neurons. Nat. Commun 1–11. [PubMed: 28232747]

Rubio-Garrido P, Perez-de-Manzo F, Porrero C, Galazo MJ, and Clasca F (2009). Thalamic Input to Distal Apical Dendrites in Neocortical Layer 1 Is Massive and Highly Convergent. Cereb. Cortex 19, 2380–2395. [PubMed: 19188274]

Saiki A, Sakai Y, Fukabori R, Soma S, Yoshida J, Kawabata M, Yawo H, Kobayashi K, Kimura M, and Isomura Y (2017). In Vivo Spiking Dynamics of Intra- and Extratelencephalic Projection Neurons in Rat Motor Cortex. Cereb. Cortex 23, 1087–1087.

Santello M, and Nevian T (2015). Dysfunction of cortical dendritic integration in neuropathic pain reversed by serotoninergic neuromodulation. Neuron 86, 233–246. [PubMed: 25819610]

Scala F, Kobak D, Bernabucci M, Bernaerts Y, Cadwell CR, Castro JR, Hartmanis L, Jiang X, Laturnus S, Miranda E, et al. (2020). Phenotypic variation of transcriptomic cell types in mouse motor cortex. Nature.

Schiller J, Schiller Y, Stuart G, and Sakmann B (1997). Calcium action potentials restricted to distal apical dendrites of rat neocortical pyramidal neurons. J. Physiol 505 (Pt 3, 605–616. [PubMed: 9457639]

Stuart GJ, and Sakmann B (1994). Active propagation of somatic action potentials into neocortical pyramidal cell dendrites. Nature 367, 69–72. [PubMed: 8107777]

Shai AS, Anastassiou CA, Larkum ME, and Koch C (2015). Physiology of Layer 5 Pyramidal Neurons in Mouse Primary Visual Cortex: Coincidence Detection through Bursting. PLOS Comput. Biol 11, e1004090–e1004090. [PubMed: 25768881]

Sheets PL, Suter BA, Kiritani T, Chan CS, Surmeier DJ, and Shepherd GMG (2011). Corticospinal-specific HCN expression in mouse motor cortex: Ih-dependent synaptic integration as a candidate microcircuit mechanism involved in motor control. J. Neurophysiol 106, 2216–2231. [PubMed: 21795621]

Sorensen SA, Bernard A, Menon V, Royall JJ, Glattfelder KJ, Desta T, Hirokawa K, Mortrud M, Miller JA, Zeng H, et al. (2015). Correlated Gene Expression and Target Specificity Demonstrate Excitatory Projection Neuron Diversity. Cereb. Cortex 25, 433–449. [PubMed: 24014670]

Sugino K, Hempel CM, Miller MN, Hattox AM, Shapiro P, Wu C, Huang ZJ, and Nelson SB (2006). Molecular taxonomy of major neuronal classes in the adult mouse forebrain. Nat. Neurosci 9, 99–107. [PubMed: 16369481]

Suter BA, Migliore M, and Shepherd GMG (2013). Intrinsic Electrophysiology of Mouse Corticospinal Neurons: a Class-Specific Triad of Spike-Related Properties. Cereb. Cortex 23, 1965–1977. [PubMed: 22761308]

Tantirigama MLS, Oswald MJ, Duynstee C, Hughes SM, and Empson RM (2014). Expression of the Developmental Transcription Factor Fezf2 Identifies a Distinct Subpopulation of Layer 5 Intratelencephalic-Projection Neurons in Mature Mouse Motor Cortex. J. Neurosci 34, 4303–4308. [PubMed: 24647950]

Takahashi N, Ebner C, Sigl-Glöckner J, Moberg S, Nierwetberg S, and Larkum ME (2020). Active dendritic currents gate descending cortical outputs in perception. Nat. Neurosci 23, 1277–1285. [PubMed: 32747790]

Tasic B, Yao Z, Graybuck LT, Smith KA, Nguyen TN, Bertagnolli D, Goldy J, Garren E, Economo MN, Viswanathan S, et al. (2018). Shared and distinct transcriptomic cell types across neocortical areas. Nature 1–41.

Tervo DGR, Hwang B-Y, Viswanathan S, Gaj T, Lavzin M, Ritola KD, Lindo S, Michael S, Kuleshova E, Ojala D, et al. (2016). A Designer AAV Variant Permits Efficient Retrograde Access to Projection Neurons. Neuron 92, 372–382. [PubMed: 27720486]

Ting JT, Daigle TL, Chen Q, and Feng G (2014). Acute Brain Slice Methods for Adult and Aging Animals: Application of Targeted Patch Clamp Analysis and Optogenetics BT - (null). In Methods in Molecular Biology, (New York, NY: Springer New York), pp. 221–242.

Tripathy SJ, Toker L, Bomkamp C, Mancarci BO, Belmadani M, and Pavlidis P (2018). Assessing Transcriptome Quality in Patch-Seq Datasets. Front. Mol. Neurosci 11, 363. [PubMed: 30349457]

Williams SR, and Stuart GJ (2000). Site independence of EPSP time course is mediated by dendritic I(h) in neocortical pyramidal neurons. J. Neurophysiol 83, 3177–3182. [PubMed: 10805715]

Zeng H, and Sanes JR (2017). Neuronal cell-type classification: challenges, opportunities and the path forward. Nat. Rev. Neurosci 18, 530–546. [PubMed: 28775344]

Zeng H, Shen EH, Hohmann JG, Oh SW, Bernard A, Royall JJ, Glattfelder KJ, Sunkin SM, Morris JA, Guillozet-Bongaarts AL, et al. (2012). Large-Scale Cellular-Resolution Gene Profiling in Human Neocortex Reveals Species-Specific Molecular Signatures. Cell 149, 483–496. [PubMed: 22500809]

Highlights

1. Species differences in the relative density of L5 ET neurons; mouse>macaque>human
2. Correspondence between physiological and transcriptomic definition of L5 classes.
3. Human L5 ET dendrites display electrogenesis during direct electrical recordings.
4. Many conserved and divergent properties of human and rodent L5 ET neurons.

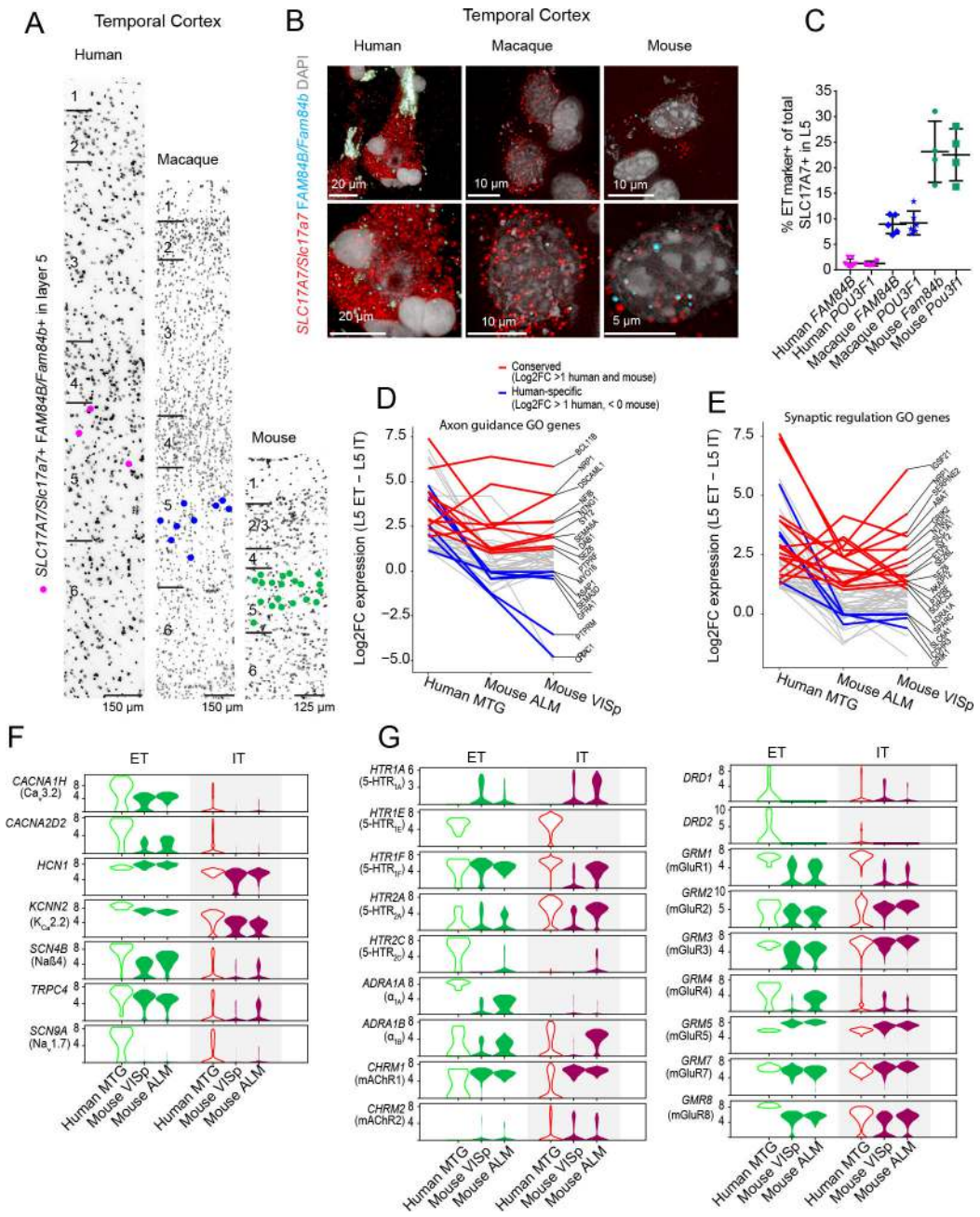

Figure 1- Cross species comparison of relative abundance and gene expression of L5 ET neurons.

A) Representative inverted images of DAPI-stained sections of human, macaque and mouse temporal cortex. Dots denote the location of cells labeled using mFISH for *FAM84B* and *SLC17A7*. Horizontal bars denote putative layer boundaries. B) Example mFISH images of *FAM84B* and *SLC17A7* labeling in L5 pyramidal neurons in human, macaque and mouse temporal cortex. C) Quantification of the proportion of *SLC17A7*+ cells expressing the ET markers *FAM84B* or *POU3F1* in temporal cortex of mouse, macaque and human expressed as a fraction of the total number of excitatory cells in L5. Individual data points are denoted by symbols. Line graphs of D) axon guidance and E) synaptic regulation related genes with expression enrichment in L5 ET versus IT neurons in human MTG (> 1 log2

fold-difference) and their respective enrichment in L5 ET neurons in mouse VISp and ALM. Notable conserved (red) and human specific (blue) genes are highlighted. Human L5 ET neuron enriched F) ion channel and G) Neuromodulator receptor gene expression and their expression in the mouse VISp and ALM.

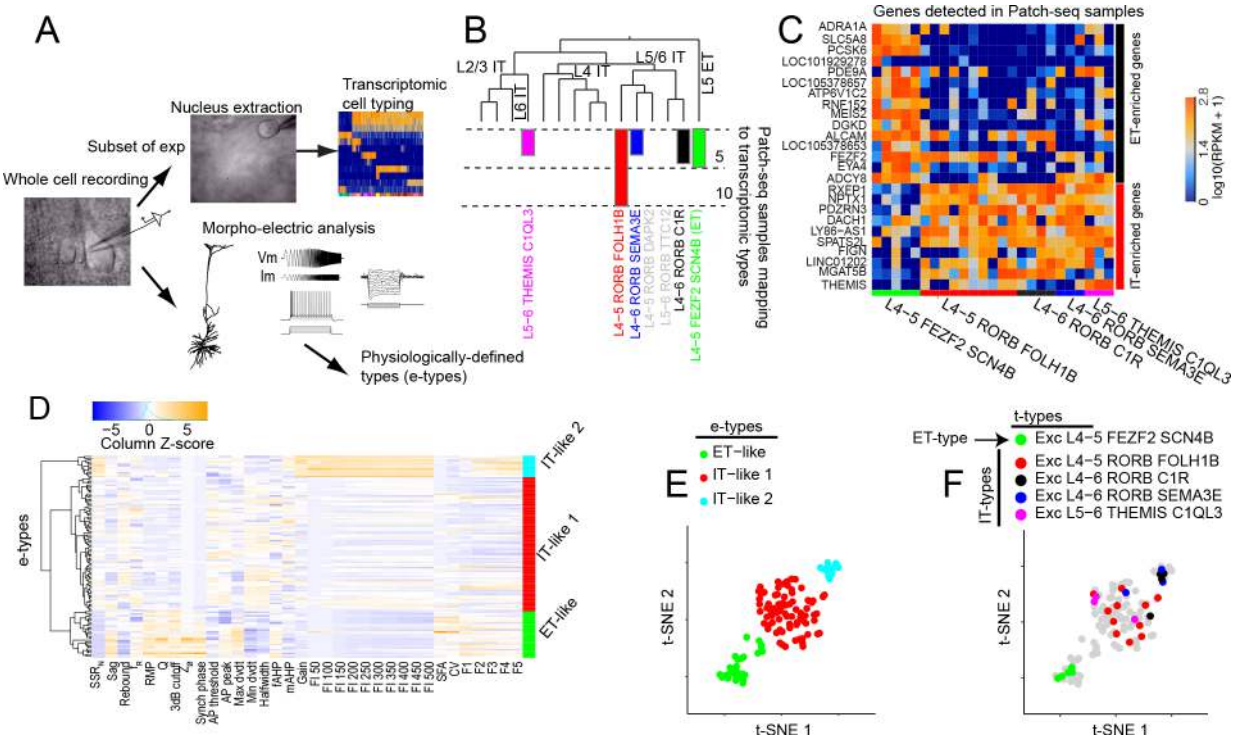

Figure 2- Patch-seq analysis reveals distinctive membrane properties of transcriptomically defined L5 ET neurons.

A) We obtained whole cell patch clamp recordings from L5 pyramidal neurons in human brain slices prepared from neurosurgical specimens. For a subset of experiments, Patch-seq analysis was performed which permitted post-hoc assignment of a transcriptomic cell type to the physiologically probed neuron. Several physiological features were extracted from all recordings and these features were used to define electrophysiological types (e-types). B) Glutamatergic transcriptomic cell types in human MTG are shown, with the number of Patch-seq samples that mapped with high confidence to each type indicated by the bar plots. Transcriptomic cell type names are adapted from Hodge et al., 2019. C) Heat map of a subset of genes detected in Patch-seq samples. Each column is a separate Patch-seq sample. ET enriched genes are highly expressed in L5 ET transcriptomic types compared to L5 IT transcriptomic types. IT enriched genes are highly expressed in L5 IT transcriptomic types compared to L5 ET transcriptomic types. Columns are color coded for transcriptomic cell types at the bottom row. D) Heat map of physiological features of human L5 pyramidal neurons. These features were used to cluster cells into physiologically defined types (e-types) using Ward's algorithm. The dendrogram represents the outcome of this clustering. tSNE projection of the features shown in D) color-coded by E) electrophysiologically-defined cell type and F) transcriptomically defined cell type.

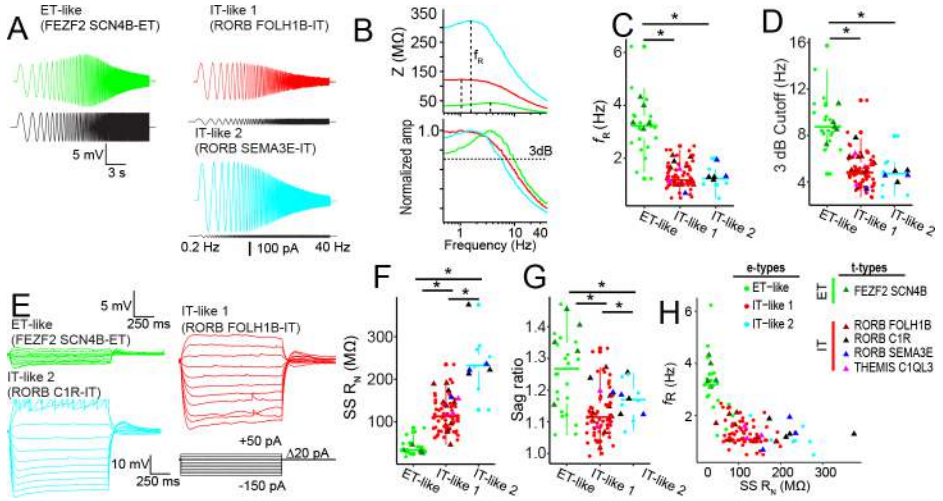

Figure 3- Subthreshold membrane properties of L5 neuron types in human MTG.

A) Example voltage response of L5 neuron types to a chirp stimulus. B) ZAP (bottom) and normalized frequency response (top) constructed from the voltage responses in A). Dashed lines indicate resonant frequency (ZAP) and 3dB cutoff (normalized curve). Pairwise comparisons of C) resonant frequency and D) 3 dB cutoff. E) Example voltage responses to a series of hyperpolarizing and depolarizing current injections. Scale is the same for ET-like and IT-like 1 sweeps, but different for IT-like 2 sweeps. Pairwise comparisons of F) Input resistance and G) Sag ratio. H) Resonant frequency as a function of input resistance. For example sweeps, mapped transcriptomic cell type is listed in parentheses. For summary plots, triangles and circles denote Patch-seq samples and physiology only samples, respectively. Legend in H) applies to all summary plots. * $p < .05$, FDR corrected Mann-Whitney U test.

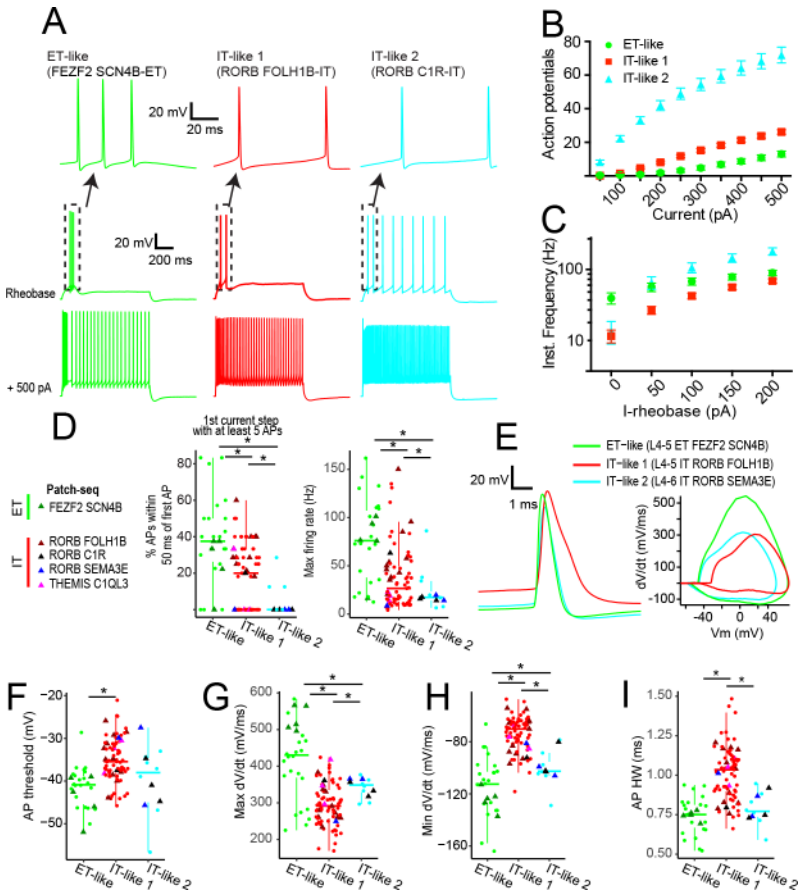

Figure 4- Suprathreshold membrane properties of L5 neuron types in human MTG.

A) Example voltage responses to near threshold current injection (middle) and +500 pA (bottom). (top)- Expanded view of spikes at near rheobase current injection. B) The number of action potentials evoked as a function of current injection amplitude. C) First instantaneous frequency plotted as a function of current injection amplitude above rheobase. D) (middle) The percentage of action potentials occurring within 50 ms of the first spike and (right) maximum instantaneous firing rate for the first current injection producing at least 5 spikes. The legend (left) applies to subsequent panels in this figure. E) Example action potentials (left) and corresponding phase-plane plots (right). Differences in F) action potential threshold, G) maximum dV/dt H) minimum dV/dt and I) action potential width at half-maximum amplitude. For example sweeps the mapped transcriptomic cell type is listed in parentheses. For box plots, triangles and circles denote Patch-seq samples and physiology only samples, respectively.* $p < .05$, FDR corrected Mann-Whitney U test. Full table of p values and effect size can be found in Tables S1,2.

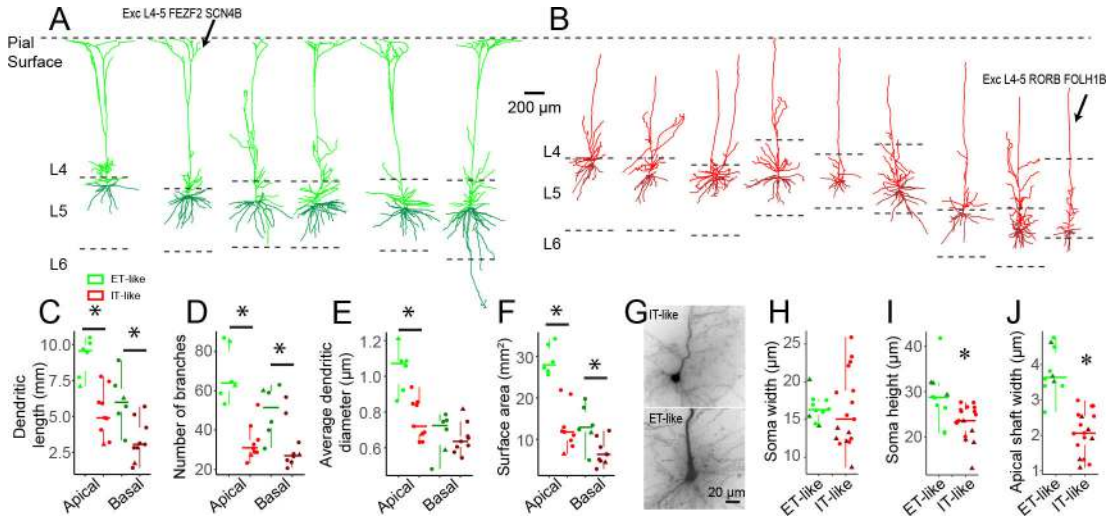

Figure 5- Morphological features of L5 ET- and IT- like neurons in human MTG.

Dendritic reconstructions of A) ET-like and B) IT-like neurons in human MTG. Apical and basal dendrites are denoted by different shades of green or red. Neurons mapping to a transcriptomic cluster from Patch-seq experiments are denoted by an arrow. Approximate layer 4/5 and layer 5/6 boundaries are denoted by dashed lines. Comparison of C) basal and apical dendritic length, D) number of basal and apical dendritic branches, E) average dendrite diameter and F) total dendritic surface area between L5 ET and IT neurons. G) Example biocytin fills of perisomatic regions for L5 ET and IT-like neurons. Comparison of H) soma width I) height and J) initial apical shaft width. For box plots, triangles denote transcriptomically defined cell types (Exc L4–5 FEZF2 SCN4B for ET-like and Exc L4–5 RORB FOLH1B for IT-like). * $p < 0.05$, FDR corrected Mann-Whitney U test.

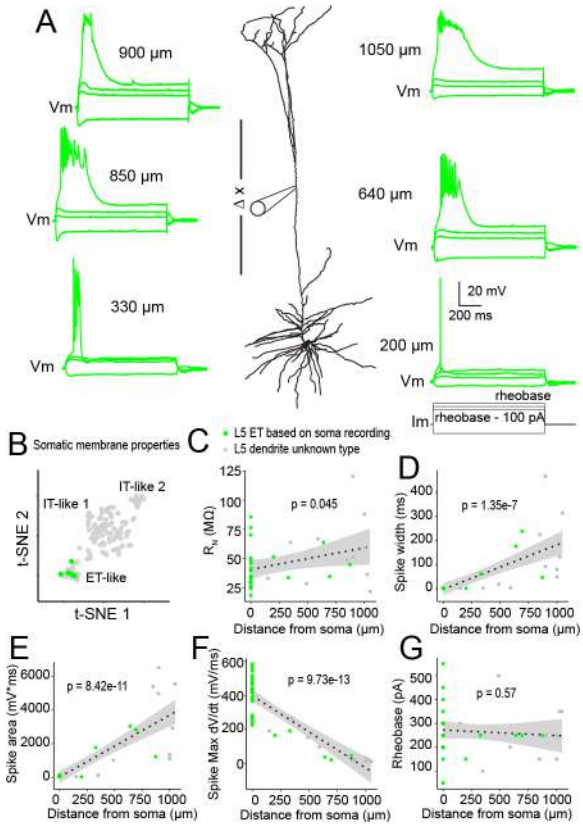

Figure 6- Putative ET neurons display strong dendritic electrogenesis.

A) Direct electrical recordings of dendritic membrane properties were performed at various distances from the soma in separate neurons. For a subset of experiments, the soma was subsequently patched with a separate electrode. Example voltage responses to hyperpolarizing and depolarizing current injections are shown. Depolarizing current injections were capable of eliciting an all-or-none plateau potential. Example sweeps are from different neurons. B) tSNE projection of somatic membrane properties of cells in which the dendritic properties were probed are shaded in green. C) Input resistance, D) spike width, E) plateau potential area, F) maximum dV/dt and G) rheobase plotted as a function of distance from soma. Values near 0 reflect thin spikes similar to the example sweep at 200 um in A. FDR corrected Pearson's correlation p values are listed for each plot. Shaded region corresponds to SEM. For D-H, green dots denote cells (n = 5) in which the somatic properties were also probed.

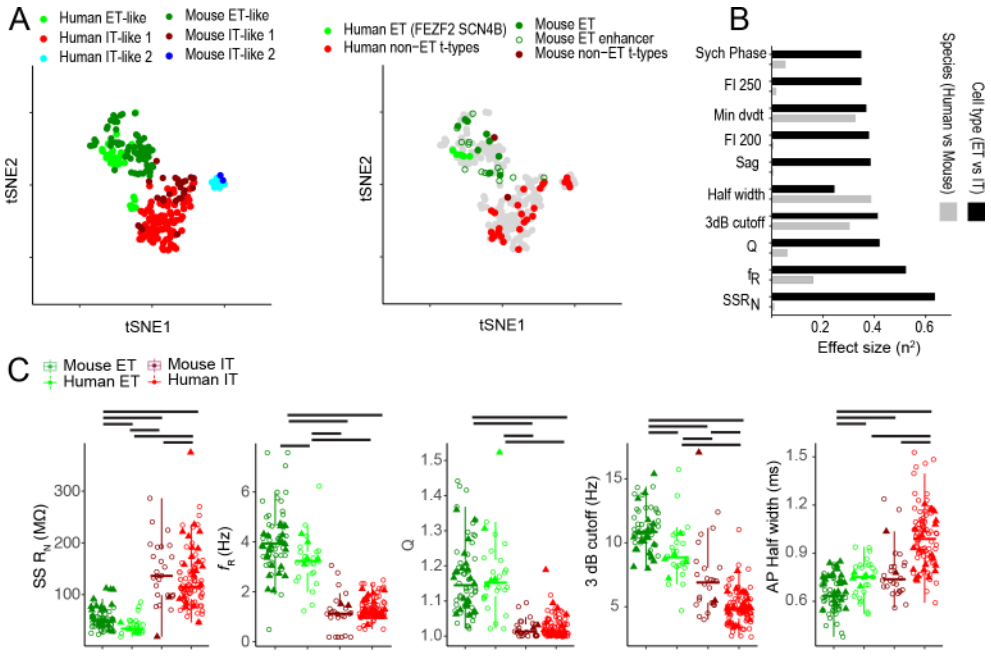

Figure 7- Cross-species comparison reveals conserved and divergent L5 ET neuron somatic membrane properties.

A) tSNE of intrinsic membrane properties for human and mouse L5 pyramidal neurons color coded by (left) physiologically-defined cell type and (right) transcriptomic cell type or labeling by an ET-enhancer virus. B) The top 10 largest effect sizes resulting from ANOVA with cell type (ET versus IT) and species (human versus mouse) as the factors. C) Physiological features plotted as a function of species and cell type for the five features with the largest effect sizes. For box plots, triangles denote neurons that mapped to a transcriptomic cell type during Patch seq experiments, or neurons labeled by an ET enhancer virus. Black bars denote $p < 0.05$, FDR corrected Mann-Whitney U test.

KEY RESOURCES TABLE

REAGENT or RESOURCE	SOURCE	IDENTIFIER
Critical Commercial Assays		
SMART-Seq v4 Ultra Low Input RNA Kit for Sequencing	Takara	634894
Nextera XT Index Kit V2 Set A-D	Nextera	FC-131- 2001,2002,2003,2004
Deposited Data		
Human MTG SMART-SEQ	Allen Brain Map	https://portal.brain-map.org/atlases-and-data/rnaseq/human-mtg-smart-seq
Mouse V1/ALM SMART-SEQ	Allen Brain Map	https://portal.brain-map.org/atlases-and-data/rnaseq/mouse-v1-and-alm-smart-seq
Patch-seq SMART-SEQ	This study	https://portal.brain-map.org/explore/classes/multimodal-characterization/human-l5-et-it
Morphological reconstructions	This study	https://download.brainimagelibrary.org/6b/f5/6bf5b41552ee560e
Experimental Models: Organisms/Strains		
macaque: macaca nemestrina	Washington National Primate Research Center	N/A
mouse: *Thy1h*–eyfp (B6.Cg-Tg(*Thy1*–YFP)-HJrs/J	The Jackson Laboratory	RRID: IMSR_JAX:003782
mouse: C57BL/6-Tg (*Pvalb*–tdTomato)15Gfng/J	The Jackson Laboratory	RRID: IMSR_JAX:027395
Human neurosurgical samples	Table S4	N/A
Oligonucleotides		
FAM84B	Advanced Cell Diagnostics	Catalog No. 537891-C2, Accession No. NM_174911.4
FAM84B	Advanced Cell Diagnostics	Accession No. NW_012011489.1, XM_011760042.2
Fam84b	Advanced Cell Diagnostics	Catalog No. 500991, Accession No. NM_001162926.1
POU3F1	Advanced Cell Diagnostics	Catalog No. 483181-C2, Accession No. NM_002699.3
Pou3f1	Advanced Cell Diagnostics	Catalog No. 436421-C2, Accession No. NM_011141.2
SLC17A7	Advanced Cell Diagnostics	Catalog No. 415611, Accession No. NM_020309.3
SLC17A7	Advanced Cell Diagnostics	Catalog No. 424831, Accession No. XM_001113054.2
Slc17a7	Advanced Cell Diagnostics	Catalog Nos. 416631 and 416631-C2, Accession No. NM_182993.2
Software and Algorithms		
Igor Pro	Wavemetrics	RRID: SCR_000325; https://www.wavemetrics.com/products/igorpro
MIES	Gouwens et al., 2019	https://github.com/alleninstitute/mies
Vaa3D	Gouwens et al., 2019	http://home.penglab.com/proj/vaa3d/
R	R Core Team, 2018	https://www.R-proiect.org/.
R analysis code	This study	10.5281/zenodo.5218234, https://doi.org/10.5281/zenodo.5218234